Journal of Theoretical Biology 394 (2016) 77–92

Contents lists available at ScienceDirect

Journal of Theoretical Biology

journal homepage: www.elsevier.com/locate/yjtbi

Influences of Allee effects in the spreading of malignant tumours

Lotte Sewalt [a,*], Kristen Harley [b], Peter van Heijster [b], Sanjeeva Balasuriya [c]

[a] Mathematisch Instituut, Leiden University, 2300 RA, Leiden, The Netherlands
[b] School of Mathematical Sciences, Queensland University of Technology, Brisbane, QLD 4001, Australia
[c] School of Mathematical Sciences, University of Adelaide, Adelaide, SA 5005, Australia

HIGHLIGHTS

- We introduce one of the first mathematical models of tumour invasion with growth thresholds.
- Only biologically relevant travelling wave fronts exist, opposing earlier models.
- Experimental observations in tumour spread are uncovered in our model.
- We show the relevance of incorporating the Allee effect in tumour spread.

ARTICLE INFO

Article history:
Received 23 April 2015
Received in revised form
10 November 2015
Accepted 30 December 2015
Available online 21 January 2016

Keywords:
Malignant tumour model
Allee effects
Travelling wave solutions
Geometric singular perturbation theory
Canard theory

ABSTRACT

A recent study by Korolev et al. [*Nat. Rev. Cancer*, 14:371–379, 2014] evidences that the Allee effect—in its strong form, the requirement of a minimum density for cell growth—is important in the spreading of cancerous tumours. We present one of the first mathematical models of tumour invasion that incorporates the Allee effect. Based on analysis of the existence of travelling wave solutions to this model, we argue that it is an improvement on previous models of its kind. We show that, with the strong Allee effect, the model admits biologically relevant travelling wave solutions, with well-defined edges. Furthermore, we uncover an experimentally observed biphasic relationship between the invasion speed of the tumour and the background extracellular matrix density.

1. Introduction

1.1. Allee effects and tumour growth

A recent article in *Nature Reviews Cancer*, (Korolev et al., 2014), has highlighted how a well-established concept in ecology—the Allee effect (Allee, 1938)—is also relevant to tumours but has yet to be incorporated into their modelling. In its strong form, the Allee effect refers to the observation that there is a population threshold below which a species has negative population growth, driving it to extinction. The weak form of the Allee effect describes a species that has small (but not negative) population growth at low populations (Courchamp et al., 2008). The ecological causes of Allee effects (which are observed within small populations) are multitudinous: the inability to find a mate; the negative impact on co-operative behaviours such as anti-predator vigilance; the increased sensitivity to demographic stochasticity; and, the lack of diversity in the extant gene pool (Courchamp et al., 1999; Keitt et al., 2001; Stephens and Sutherland, 1999). Evidence for the strong (Berger, 1990; Courchamp and MacDonald, 2001; Groom, 1998; Johnson et al., 2006; Lamont et al., 1993) and weak (Allee, 1938; Angulo et al., 2007; Davis et al., 2004; Tang et al., 2014; Taylor et al., 2004) Allee effects are plentiful across many taxa; additional reviews are available in Gregory et al. (2010); Kramer et al. (2009). Consequently, there is a proliferation of mathematical models of the Allee effect in ecology (e.g. Balasuriya, 2010; Balasuriya and Gottwald, 2010; Cushing, 2014; Hart and Aviles, 2014; Kribs-Zaleta and Mitchell, 2014; Lewis and Kareiva, 1993; Potapov and Rajakaruna, 2013; Yamamichi et al., 2014). While studies in ecology often worry about factors that might push a threatened species below the (strong) Allee threshold and thereby towards extinction (e.g. Sanderson et al., 2014), an intriguing possibility in cancer research is whether the Allee effect could be harnessed for controlling or negating the growth of cancerous cells (Korolev et al., 2014), consonant with recent experiments in bacteria (Smith et al., 2014).

While seldom stated, hints of the Allee effect are numerous in the cancer research literature. Firstly, at the most anecdotal level, a tumour is only deemed threatening if it is above a certain size, which is an

* Corresponding author. Tel.: +31 71 527 70 46.
E-mail address: lotte@math.leidenuniv.nl (L. Sewalt).

http://dx.doi.org/10.1016/j.jtbi.2015.12.024
0022-5193/

implicit presumption of a strong Allee threshold. More concrete illustrations are available in clinical trials for papillary and follicular thyroid cancers (Machens et al., 2005), in which risk-of-spread versus initial tumour size figures indicate that the risk is effectively zero until a minimum primary tumour size is reached. Secondly, studies of tumour dormancy suggest the presence of mechanisms such as a restrictive apoptosis/proliferation equilibrium (a cell density at which natural cell death balances new cell production) or a minimum angiogenic potential requirement for blood vessel formation in the tumour (Ruppender et al., 2013). Such biological considerations translate to the inability of the tumour to grow unless a strong Allee threshold is reached. Thirdly, it has been shown experimentally that in the growth of blebs (spherical protrusions forming along the front boundary of tumours), there is a minimum surface tension below which the blebs cannot expand (Tinevez et al., 2009). Since this surface tension is governed by a variety of poorly understood factors such as available myosin (Tinevez et al., 2009), the existing microenvironment can be thought of as essentially imposing an Allee effect. Fourthly, Axelrod et al. (2006) and Pienta et al. (2008) provide evidence of the co-operation between nearby subclones in the early evolution of tumours through the production and exchange of growth factors. Since co-operation is adversely impacted at low populations, tumour cells must—as in ecological systems—encounter the Allee effect. Fifthly, deleterious mutations accumulate more in smaller tumours (Korolev et al., 2014), thereby driving the population to extinction with much higher probability than larger tumours. Sixthly—and at a much broader level—the very fact that cancers depend on genetic heterogeneity, mutations and subsequent evolution (Burrell et al., 2013; Greaves and Maley, 2012; Merlo et al., 2006), pinpoints the necessity of having a large enough gene pool for successful growth, that is, the requirement of an Allee effect.[1] For example, numerical results from a recent integral equation model that models the number of cells in clones with different mutation rates, indicate that there is a threshold genetic mutation rate below which the cancer cells suffer extinction (Amor and Solé, 2014). It is important to note that most evolutionary models of cancer (see the reviews by Merlo et al., 2006 and Michor et al., 2004) neglect the spatial structure, which is problematic given that tumours are clinically classified depending on their shape (Connolly et al., 2000). One way of incorporating genetic mutation information within a spatial spreading model is to treat the stochastic mutations as creating an effective strong Allee threshold.

There are a variety of tumour growth models which examine the roles of additional effects such as acidity (Gatenby and Gawlinski, 1996; McGillen et al., 2014; Bertuzzi et al., 2010), adhesion (Chaplain et al., 2011; Gerisch and Chaplain, 2008; Sherratt et al., 2009), non-local interactions (Szymanska et al., 2009; Gerisch and Chaplain, 2008), cell plasticity in proliferation versus migration (Gao et al., 2005; Hatzikirou et al., 2012; Tektonidis et al., 2011; Martínez-González et al., 2012), in a range of tumour types. Most models fall into two classes: those which simulate a network of cells (Tektonidis et al., 2011; Hatzikirou et al., 2012), and those which rely of continuum modelling (e.g. Chaplain et al., 2011; McGillen et al., 2014; Szymanska et al., 2009; Gatenby and Gawlinski, 1996; Sherratt et al., 2009; Martínez-González et al., 2012), although some models that make a connection between the two exist, (e.g. Painter and Hillen, 2013; Bellomo et al., 2010; Engwer et al., 2015). Very recently, a spatio-temporal tumour cell growth model incorporating micro-environmental influences has been studied. That analysis reveals an Allee effect depending on the cell motility versus local cell density, (Böttger et al., 2015).

[1] This is stating that genetic diversity produces an implicit Allee effect, different from studies on the impact of a *separately imposed* Allee effect on genetic diversity (Wittman et al., 2014a,b).

1.2. A new model for malignant tumour invasion

In light of this emergent viewpoint on the relevance of the Allee effect in cancers, we offer in this paper, one of the first cancer spreading model that explicitly includes the Allee effect. Specifically, we examine how the inclusion of the Allee effect changes conclusions in comparison to the commonly used logistic growth model. For our comparison – the first of its kind – we choose to examine a model of a malignant, solid tumour invading through the extracellular matrix (ECM) via hapto- or chemotaxis, as opposed to the more complex, metastatic dissemination regime (Wells et al., 2013). In particular, our analysis applies to the spread of tumours in which hapto- or chemotaxis is the dominant mechanism of cell migration, such as melanoma (Marchant et al., 2000; Perumpanani and Byrne, 1999). We focus on the behaviour of the tumours on a long time scale; we do not analyse the transient dynamics.

We assume that an invasive tumour front can be modelled, mathematically, by a travelling wave solution (TWS) with constant speed c. TWSs correspond to stationary solutions in an appropriately moving frame and are defined on a one-dimensional, unbounded spatial domain. While this choice of domain is a simplification of the geometry of tumour invasion, it is a reasonable approximation, while still yielding a model that is amenable to mathematical analysis.

We build on a model of malignant tumour invasion derived in Perumpanani et al. (1999) and subsequently studied in Harley et al. (2014a); Marchant et al. (2000). In these articles, a logistic growth term is used to model the growth of the cancer cells (see Section 1.4); Allee effects are neglected. Here, we replace this logistic growth term with an Allee growth term and study the existence of TWSs of the following dimensionless model for malignant tumour invasion (see Section 2 for the derivation):

$$\begin{aligned}\frac{\partial u}{\partial t} &= \overbrace{-u^2 w}^{\text{proteolysis}} + \overbrace{\varepsilon\beta\frac{\partial^2 u}{\partial x^2}}^{\text{diffusion}},\\ \frac{\partial w}{\partial t} &= \underbrace{f(u,w)}_{\text{growth}} - \underbrace{\frac{\partial}{\partial x}\left(\frac{\partial u}{\partial x}w\right)}_{\text{hapto-/chemotaxis}} + \underbrace{\varepsilon\frac{\partial^2 w}{\partial x^2}}_{\text{diffusion}},\end{aligned} \tag{1}$$

with

$$f(u,w) = f_{\text{Allee}}(w;\alpha) := w(1-w)(w-\alpha), \quad |\alpha| < 1. \tag{2}$$

The dependent variables $u \geq 0$ and $w \geq 0$ represent the dimensionless ECM and cancer cell densities, respectively. The independent variables $t > 0$ and $x \in \mathbb{R}$ represent time and one-dimensional space, respectively. Both species are assumed to diffuse slowly, which is modelled by the small parameter ε: $0 \leq \varepsilon \ll 1$. We further assume that the ECM diffuses more slowly than the cancer cells: $0 \leq \beta \leq 1$ and β independent of ε. Observe that our analysis is also able to capture the situation of the ECM not diffusing, i.e. $\beta = 0$. The observed migration of the cancer cells up the gradient of ECM is modelled by the hapto- or chemotaxis term. As the cancer cells migrate they break down the ECM; this is modelled by the proteolysis term. The cubic function describing the growth of the cancer cells, (2), models the Allee effect, with different values of α corresponding to different strengths. Consistent with the definition in Section 1.1, the Allee effect modelled by (2) describes the following.

A positive α models the strong Allee effect. Since the carrying capacity of the cancer cell density has been scaled to one in (2), we require $\alpha < 1$. The strong Allee effect imposes a growth threshold on the tumour, whereby the cancer cell population only increases (at a given location) if $\alpha < w < 1$, since otherwise $f_{\text{Allee}} \leq 0$. See also Fig. 1. In the context of tumour invasion, $\alpha \gtrapprox 0$ is the most appropriate representation of the strong Allee effect as it is unlikely that a large threshold value (relative to the carrying capacity) is needed for the proliferation of cancer cells.

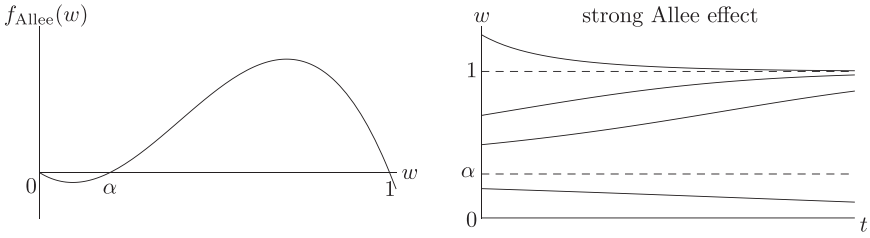

Fig. 1. Left-hand panel: Sketch of $f_{\text{Allee}} = w(1-w)(w-\alpha)$ for $0<\alpha<1$. Observe that $f_{\text{Allee}}>0$ for $\alpha<w<1$. Right-hand panel: Sketch of the solutions to $w' = w(1-w)(w-\alpha)$ with $0<\alpha<1$. Initial conditions larger than α approach the carrying capacity (which is scaled to one), while initial conditions smaller than α die out and approach $w=0$.

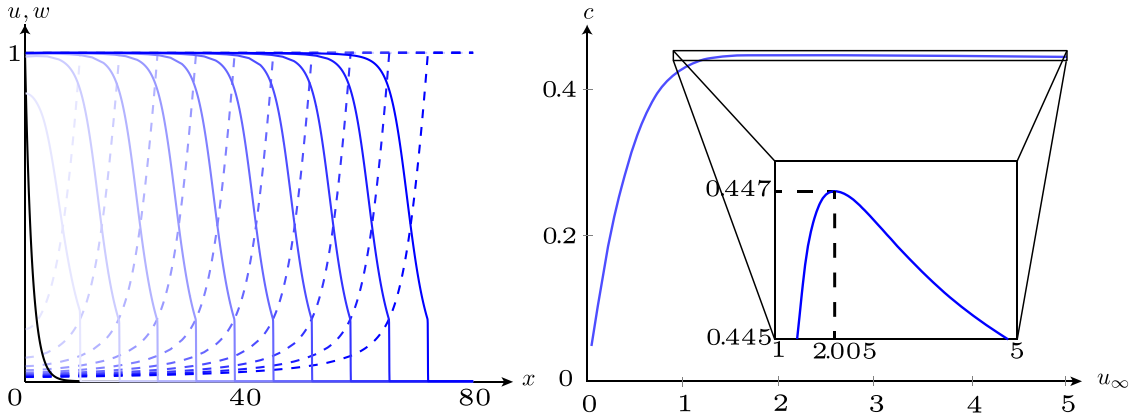

Fig. 2. Left-hand panel: A *Type III wave* with a biologically justified, well-defined edge and speed $c\approx 0.43$, obtained by numerically simulating (1)–(2) with $\varepsilon = 0.001$, $\alpha = 0.05$ and $\beta = 0.5$. The dashed lines correspond to u-profiles and the solid lines to w-profiles, with solutions plotted at $t=0$ (black), 16 (lightest), 32,…, 160 (darkest). Right-hand panel: The leading order ($\varepsilon = 0$) component of the speed of travelling wave solutions of (1)–(2) (c) versus the background ECM density (u_∞), with $\alpha = 0.05$, illustrating a biphasic relationship.

A negative α models the weak Allee effect. Unlike the strong Allee effect, the weak Allee effect does not impose a growth threshold. Instead, it models a population with a growth rate that is initially positive and increases with population increase for *small* populations, until crowding effects take over and cause the growth rate to decrease with further population increase. Hence, we require $\alpha > -1$, with $\alpha \gtrapprox -1$ corresponding to the most appropriate representation of the weak Allee effect.

For further discussion and more precise definitions of the strong and weak Allee effects, see Courchamp et al. (2008) and Appendix A.

1.3. Main results

The focus of this paper is to compare the Allee model (1)–(2) with the logistic model, developed in Perumpanani et al. (1999), with respect to its ability to capture the behaviour of malignant tumour invasion. Furthermore, we compare our results to a different modification of the logistic model, studied in Marchant et al. (2006), where competition between the species is included in $f(u,w)$ in (1). For convenience, we refer to (1)– (2) with $\alpha \gtrapprox 0$ and $\alpha \gtrapprox -1$ as the strong and weak Allee models, respectively. We present evidence that the strong Allee model provides a better model of tumour invasion than these previously proposed models, while the weak Allee model provides no significant improvement. The following sections provide a summary of the main results that lead to these conclusions.

1.3.1. Strong Allee model

For the strong Allee model, we find that:

- Only invasive tumour fronts with well-defined edges (Marchant et al., 2006) (so-called *Type III waves*, see Section 1.4) exist, rather than the whole family that exists for the previously studied models of malignancies such as melanoma (Harley et al., 2014a; Perumpanani et al., 1999; Marchant et al., 2000, 2006); and,
- A non-monotonic (biphasic) relationship between the background ECM density and the invasion speed of the tumour is evident, consistent with the experiments on a HT1080 fibrosarcoma cell line invading collagen gels as reported in Perumpanani and Byrne (1999); Marchant et al. (2006). In contrast, models without the Allee effect predict a monotonic relationship (Harley et al., 2014a; Perumpanani et al., 1999; Marchant et al., 2000). See in particular Fig. 11 in Harley et al. (2014a).

These results are illustrated in Fig. 2. The numerical method used to simulate (1)–(2) uses a vertex-centred finite volume discretisation in space, with upwinding to approximate u and w at the faces of the control volumes, on a linear mesh with $\Delta x = 1/80$. The resultant ODEs are integrated in time using `MATLAB`'s inbuilt ODE solver `ode45` (which uses a variable-order Runge–Kutta algorithm with adaptive timestepping).

1.3.2. Weak Allee model

In contrast, the main result relating to the weak Allee model is that it offers no notable benefits over the previously studied models for tumour invasion such as melanoma and, so, due to its added complexity, is a less preferable model of malignant invasion. Consequently, we omit the derivation of the results from the main body of the paper; we present them briefly in Appendix B. The key findings that lead to our conclusion are as follows:

- There exists a family of invasive tumour fronts (so-called *Type I–IV waves*), which includes some that have non-sharp fronts but that appear (numerically) to be stable and, hence, observable within the system.
- The relationship between the background ECM density and the invasion speed of the tumour fronts with sharp edges is

monotonically increasing, contrary to an experimentally observed biphasic relationship (Perumpanani and Byrne, 1999).

1.4. Comparison with results for previous models

In the models for malignant tumour invasion studied in Harley et al. (2014a); Marchant et al. (2000); Perumpanani and Byrne (1999); Perumpanani et al. (1999), the cancer cells are assumed to grow logistically, governed by the dimensionless kinetic function

$$f(u,w)=f_{\text{logistic}}(w):=w(1-w). \tag{3}$$

In the model studied in Marchant et al. (2006), an interaction term between the ECM (u) and cancer cells (w) is added to (3) to signify the competition for space between the two species. Subsequently, the growth of the cancer cells is governed by the dimensionless kinetic function

$$f(u,w)=f_{\text{competition}}(w):=w(1-w)-\gamma uw. \tag{4}$$

Thus, the models studied previously are (1), with (3) or (4) in place of (2).[2] Henceforth, for convenience, we refer to the former as the logistic model and the latter as the competition model.

In Harley et al. (2014a), it is shown that the logistic model admits a continuous family of travelling wave solutions (TWSs). This family is classified into four distinct types, according to qualitative differences in the cancer cell density profiles, in the singular limit $\varepsilon\to 0$; see Fig. 3. A *Type I wave* has a smooth, exponentially decaying cancer cell density profile. A *Type II wave* has a cancer cell density profile with a shock but that remains positive and decays exponentially to zero as $x\to\infty$. A *Type III wave* has a cancer cell density profile with a shock and semi-compact support. A *Type IV wave* has a cancer cell density profile with a shock and that decays exponentially to zero as $x\to\infty$ but with densities that are negative after the shock. Preliminary numerical results suggest that the Type I–III waves are stable, in the sense that they are observable in the system, while the Type IV waves are not (Harley et al., 2014a).

Remark 1. The labelling of the four wave types depicted in Fig. 3 refers to those waves identified in Harley et al. (2014a) for the logistic model. However, the classifications that underpin this terminology apply more generally, for example, to TWSs of (1) with $0\le\varepsilon\ll 1$ and $0\le\beta\le 1$. Thus, we adopt the labels Type I–IV and henceforth use them to refer to any waves with equivalent features to those described in Harley et al. (2014a), outlined above.

A similar family of Type I–IV waves exists for the competition model, studied in Marchant et al. (2006).[3] Moreover, numerical simulations suggest that in certain, broad parameter regimes, the Type I–III waves are stable and, hence, observable in the system.

From a biological perspective, Type III waves are considered to be most realistic for tumours which are expected to possess a well-defined edge; such as melanomas, see for example Marchant et al. (2006). In contrast to the logistic, competition and weak Allee models, the strong Allee model automatically *selects* tumours with sharply defined edges.

In Perumpanani and Byrne (1999), a *biphasic relationship* between the background collagen (the predominant ingredient in ECM) density and the invasion speed of malignant tumours is observed experimentally. These experimental results indicate that the invasion speeds of malignant tumours do not increase monotonically with the background collagen (and, hence, ECM) density. Instead, there is some critical density up to which the invasion speed increases but over which the invasion speed decreases. The competition model was proposed in Marchant et al. (2006) to mathematically replicate this biphasic relationship, which is not a feature of the logistic model (Harley et al., 2014a; Marchant et al., 2000, 2006). The logistic model exhibits a monotonically increasing relationship between the speed of the Type III waves c_{III} and the background ECM density u_∞, similar to the weak Allee model. By studying only the Type III waves, the desired biphasic relationship is revealed in Marchant et al. (2006). Mathematically, this result is facilitated by the existence to two Type III waves, with different u_∞, for certain, fixed speeds.

1.5. Outline

The remainder of the paper is set out as follows. In Section 2, we derive the dimensionless model (1) from a dimensional model for malignant tumour invasion proposed in Perumpanani et al. (1999). In Section 3, we set up the mathematical framework that is required to prove the main results of the strong Allee model, described in Section 1.3.1. We prove (in a mathematically rigorous way) that the strong Allee model only admits Type III travelling wave solutions. The framework we follow exploits the separation of scales between the hapto- or chemotaxis and diffusion terms. It is based on that described in Wechselberger and Pettet (2010) and uses geometric singular perturbation theory (GSPT) (Hek, 2010; Jones, 1995; Kaper, 1999) and canard theory (Benoit et al., 1981; Krupa and Szmolyan, 2001; Szmolyan and Wechselberger, 2001; Wechselberger, 2012). The results for the strong Allee model are further analysed in Section 4, including the biological implications of our findings in relation to previously studied models. In Section 5, we discuss the extension of our results to a more general class of models, the limitations of our work and topics for future research.

Remark 2. The mathematical derivation contained within Section 3 is not prerequisite to following the arguments and discussions contained within the subsequent sections. Thus, we invite the less mathematically inclined reader to skip over it.

2. Model derivation

Our decision to study (1) is inspired by Perumpanani et al. (1999), where, after a quasi-steady state approximation, the following dimensional model of malignant tumour invasion is studied (using the notation in Harley et al., 2014a):

$$\begin{aligned}\frac{\partial\hat{u}}{\partial\hat{t}}&=-k_4\hat{u}^2\hat{w},\\ \frac{\partial\hat{w}}{\partial\hat{t}}&=\hat{k}_1\hat{w}(k_2-\hat{w})-k_3\frac{\partial}{\partial\hat{x}}\left(\frac{\partial\hat{u}}{\partial\hat{x}}\hat{w}\right),\end{aligned} \tag{5}$$

Here, $\hat{x}$ represents one-dimensional space (in metres, m) and $\hat{t}$ represents time (in seconds, s). The dependent variable $\hat{u}$ (kg m^{-3}) represents the ECM density and $\hat{w}$ (cells m^{-3}) represents the cancer cell density. Diffusion of the species is assumed to be small and therefore neglected. The parameter $k_3>0$ ($\text{m}^5\,\text{kg}^{-1}\,\text{s}^{-1}$) measures the strength of the hapto- or chemotaxis term, which models the observed migration of cancer cells up the gradient of ECM. The nonlinear function $-k_4\hat{u}^2\hat{w}$ models the degradation of the ECM via proteolysis at rate $k_4>0$ ($\text{m}^6\,\text{kg}^{-1}\,\text{cells}^{-1}\,\text{s}^{-1}$).[4] The proliferation of the cancer cells is modelled by the nonlinear function $\hat{k}_1\hat{w}(k_2-\hat{w})$: without spatial influences and independent of the other species, the cancer cells grow logistically to their carrying capacity $k_2>0$

[2] In Marchant et al. (2000), Perumpanani et al. (1999), Marchant et al. (2006), it is assumed, for simplicity, that $\varepsilon=0$. In Harley et al. (2014a), $\beta=1$.

[3] Only Type III waves are considered in Marchant et al. (2006) but, using methods developed in Wechselberger and Pettet (2010) and used in Harley et al. (2014a) and here, it can be shown that Type I, II and IV waves also exist.

[4] An enzyme—protease—that is produced in the presence of cancer cells, breaks down the ECM in a process called proteolysis. However, the protease reaction evolves on a much faster time scale than the other processes within the tumour and so a quasi-steady state reduction is applied; see Perumpanani et al. (1999) for more details.

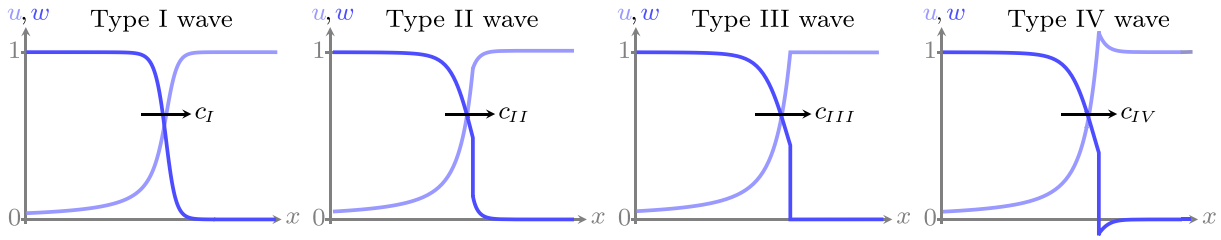

Fig. 3. Schematics of the four types of travelling wave solutions discussed in this paper. This figure is an adaptation of Fig. 6 in Harley et al. (2014a). Copyright © 2014 Society for Industrial and Applied Mathematics. Reprinted with permission. All rights reserved.

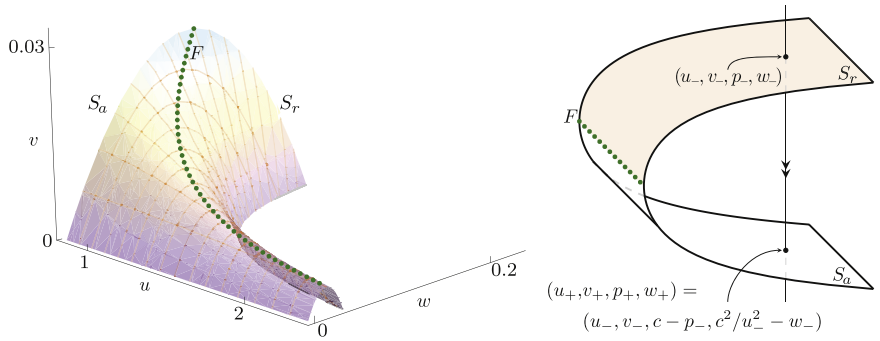

Fig. 4. The critical manifold S, defined in (14). S is folded around the fold curve F, defined in (15) and represented by the green dotted line. It is symmetric in w around F, with one repelling side (S_r) and one attracting side (S_a). Left-hand panel: Projection of the S into (u, v, w)-space, highlighting the folded structure. Right-hand panel: A schematic of S and an example of a flow connecting a point on S_r to the corresponding point on S_a. This is an adaptation of Fig. 4 in Harley et al. (2014b). © IOP Publishing & London Mathematical Society. Reproduced with permission. All rights reserved. (For interpretation of the references to color in this figure caption, the reader is referred to the web version of this paper.)

(cells m^{-3}), with (constant) proliferation rate $\hat{k}_1 k_2 > 0$ (s^{-1}). We refer to Perumpanani et al. (1999) for a more detailed derivation of (5).

We wish to study the influence of incorporating an Allee effect into the description of the growth of the cancer cells. We assume that the same nonlinearity for proteolysis but replace the cancer cell growth function with an Allee term. Following Wechselberger and Pettet (2010), we reintroduce the small amount of diffusion of both the ECM and cancer cells that was neglected in (5). With these adaptations, the model under investigation becomes

$$\frac{\partial \hat{u}}{\partial \hat{t}} = -k_4 \hat{u}^2 \hat{w} + D_1 \frac{\partial^2 \hat{u}}{\partial \hat{x}^2},$$

$$\frac{\partial \hat{w}}{\partial \hat{t}} = k_1 \hat{w}(k_2 - \hat{w})(\hat{w} - k_6) - k_3 \frac{\partial}{\partial \hat{x}}\left(\frac{\partial \hat{u}}{\partial \hat{x}} \hat{w}\right) + D_2 \frac{\partial^2 \hat{w}}{\partial \hat{x}^2}, \tag{6}$$

with $k_i > 0$ for $i \in \{1, \ldots, 5\}$, $|k_6| < k_2$ and $0 \le D_1 \le D_2$ ($m^2\ s^{-1}$). We will allow for the ECM to have both no diffusion ($D_1 = 0$), and small diffusion, in comparison to the cancer cells.

Here, k_2 (cells m^{-3}) is still the carrying capacity of the cancer cell density, while $k_1 k_2 k_6(\hat{w}/k_6 - 1)$ (s^{-1}) is the (density dependent) proliferation rate. This density dependent proliferation rate, in contrast to the constant proliferation rate assumed by logistic growth, is the main difference between the two models, (5) and (6). For $k_6 > 0$, k_6 (cells m^{-3}) represents a growth threshold, below which the cancer cell density decreases, consistent with the strong Allee effect. For $k_6 < 0$, the interpretation of k_6 is less clear. However, the effect of the term $(1 + \hat{w}/(-k_6))$ is to increase the proliferation rate, relative to the (constant) rate $k_1 k_2 (-k_6)$, with this increase more pronounced as the cancer cell density increases, consistent with the weak Allee effect; see Courchamp et al. (2008) for further discussion of the weak (and strong) Allee effects and their mathematical representation.

We introduce

$$u = \frac{\hat{u}}{U}, \quad w = \frac{\hat{w}}{W}, \quad t = \frac{\hat{t}}{T}, \quad x = \frac{\hat{x}}{X}, \tag{7}$$

with

$$U = \frac{k_1 k_2}{k_4}, \quad W = k_2, \quad T = \frac{1}{k_1 k_2^2}, \quad X = \sqrt{\frac{k_3}{k_2 k_4}},$$

and define

$$\alpha := \frac{k_6}{k_2} < 1, \quad \beta := \frac{D_1}{D_2} \le 1, \quad \varepsilon := \frac{k_4}{k_1 k_2 k_3} D_2.$$

This nondimensionalisation transforms (6) to (1)–(2), restated here for convenience:

$$\frac{\partial u}{\partial t} = -u^2 w + \varepsilon\beta \frac{\partial^2 u}{\partial x^2},$$

$$\frac{\partial w}{\partial t} = w(1 - w)(w - \alpha) - \frac{\partial}{\partial x}\left(\frac{\partial u}{\partial x} w\right) + \varepsilon \frac{\partial^2 w}{\partial x^2}, \tag{8}$$

with $(x, t) \in (\mathbb{R}, \mathbb{R}^+)$, $|\alpha| < 1$, $0 \le \beta \le 1$ and $0 < \varepsilon \ll 1$. The new variables u, w, x and t, and parameters α, β and ε are dimensionless; see Appendix C. Moreover, α and β are assumed to be $\mathcal{O}(1)$ with respect to ε: (loosely speaking) for $\alpha, \beta > 0$ they are independent of ε and do not approach zero in the limit $\varepsilon \to 0$. Due to the choice of nondimensionalisation, the carrying capacity of the cancer cells has been scaled to one and the strength of the Allee effect is solely measured by the parameter α.

The significant reduction in the number of parameters from eight in (6) to three in (8) makes the latter (dimensionless) model considerably more amenable to mathematical analysis.

3. Type III travelling wave solutions

In this section, we provide the mathematical foundation to derive the results for the strong Allee model ((8) with $\alpha \gtrapprox 0$, $0 \le \beta \le 1$ and ε sufficiently small), stated in Section 1.3.1. We prove that this model only admits Type III travelling wave solutions (TWSs).

In the strong Allee model the homogeneous equilibria $(u, w) = (0, 1)$ and $(u_\infty, 0)$, with $u_\infty \in \mathbb{R}^+$, represent an all-cancer state and a

cancer-free state, respectively. When studying invasive tumour fronts, we are interested in connections between these two states. From a mathematical standpoint, we study the existence of right-moving TWSs of (1)–(2) that travel with constant speed: $c>0$. Such solutions correspond to stationary solutions in the moving frame $z=x-ct$ and so satisfy

$$\begin{aligned} -cu_z &= -u^2w+\varepsilon\beta u_{zz},\\ -cw_z &= w(1-w)(w-\alpha)-(u_zw)_z+\varepsilon w_{zz}, \end{aligned} \tag{9}$$

TWSs also satisfy the asymptotic boundary conditions

$$\lim_{z\to-\infty}(u,w)=(0,1),\quad \lim_{z\to\infty}(u,w)=(u_\infty,0),\quad u_\infty\in\mathbb{R}^+, \tag{10}$$

where u_∞ represents the (variable) background ECM density, as in Harley et al. (2014a). Thus, TWSs of (1)–(2) or (8) correspond to heteroclinic connections (HCs) of (9) that satisfy (10).

Theorem 3.1. *For $0<\varepsilon\ll 1$ sufficiently small and $0<\alpha<1$, $0\le\beta\le 1$ and $\mathcal{O}(1)$ with respect to ε, the only possible solution of (9)–(10) corresponds to a Type III travelling wave solution of (1)–(2).*

We prove Theorem 3.1 using a method outlined in Wechselberger and Pettet (2010), which is subsequently used in Harley et al. (2014a) to study the logistic model. The foundation of this method lies in geometric singular perturbation theory (GSPT) (Hek, 2010; Jones, 1995; Kaper, 1999), which provides a geometric approach to singular perturbation problems. The benefit of using GSPT lies in the rigorous theory that underpins it, which exploits the geometric structure embedded in models such as (1) and allows us to prove that the leading order solutions we construct are good approximations of the full solutions with $0<\varepsilon\ll 1$. Canard theory (Benoit et al., 1981; Krupa and Szmolyan, 2001; Szmolyan and Wechselberger, 2001; Wechselberger, 2012) is also used when the standard GSPT, known as Fenichel theory (Fenichel, 1979; Jones, 1995), becomes invalid due to a loss of normal hyperbolicity of the critical manifold. Conditions on the vector field of (9) that guarantee the existence of Type III TWSs are also derived.

3.1. Set-up

System (9) is singularly perturbed, due to the different asymptotic scalings of the diffusion and hapto- or chemotaxis terms, with perturbation parameter $0\le\varepsilon\ll 1$. Singularly perturbed systems exhibit an inherent separation of scales. In Figs. 2 and 3, for example, we observe two spatiotemporal scales: the *fast scale* captures the dynamics where rapid changes occur, which, in the singular limit, correspond to shocks in the solutions; and, the *slow scale* relates to the dynamics away from the shocks (in the singular limit), or where less rapid changes occur.

The separation of slow and fast behaviour becomes more evident when we write the w-equation of (9) as a balance law

$$(\varepsilon w_z-u_zw+cw)_z=-w(1-w)(w-\alpha).$$

So, we define two new variables,

$$p:=u_z\quad\text{and}\quad v:=\varepsilon w_z-\mathrm{pw}+\mathrm{cw},$$

(see Harley et al., 2014a and Wechselberger and Pettet, 2010 for a further rationale behind the rescaling above). This way, we can write (9) as a four-dimensional system of first-order ordinary differential equations (ODEs):

$$\begin{aligned} u_z &= p,\\ v_z &= -w(1-w)(w-\alpha),\\ \varepsilon p_z &= \frac{1}{\beta}(u^2w-cp),\\ \varepsilon w_z &= v+(p-c)w. \end{aligned} \tag{11}$$

For $\beta=0$, the equation for p in (11) becomes singular. This has to do with the fact that the u-equation of (9) is only first order for $\beta=0$, as opposed to second order for $\beta>0$. We assume from now on that $\beta>0$, and discuss the proof of Theorem 3.1 for $\beta=0$ (which goes along the same lines as for $\beta>0$) in some more detail in Remark 4. Following standard terminology from geometric singular perturbation theory (see for example Jones, 1995; Kaper, 1999) we label (11) the *slow system*, with z the *slow travelling wave coordinate*. Provided $\varepsilon\neq 0$, we can equivalently write (11) in terms of the fast scale by introducing the *fast travelling wave coordinate*, $y=z/\varepsilon$:

$$\begin{aligned} u_y &= \varepsilon p,\\ v_y &= -\varepsilon w(1-w)(w-\alpha),\\ p_y &= \frac{1}{\beta}(u^2w-cp),\\ w_y &= v+(p-c)w. \end{aligned} \tag{12}$$

So, (u,v) are the slow variables and their equations determine the dynamics away from the shock, while the equations for the fast variables (p,w) determine the dynamics around the shock. While (11) and (12) are equivalent for $\varepsilon\neq 0$, in the singular limit $\varepsilon\to 0$, they reduce differently depending on the spatiotemporal scale. In Sections 3.2–3.3, we study the singular limits of (12) and (11), respectively. The results of these sections determine the leading order behaviour of the heteroclinic connections in the appropriate regimes. In Section 3.4, the results from Sections 3.2–3.3 are combined to prove Theorem 3.1.

3.2. Layer problem

On the fast scale, taking the singular limit ($\varepsilon\to 0$) of the so-called *fast system*, (12), yields a two-dimensional ODE system, termed the *layer problem*:

$$\begin{aligned} p_y &= \frac{1}{\beta}(u^2w-cp),\\ w_y &= v+(p-c)w, \end{aligned} \tag{13}$$

with two parameters $u,v\in\mathbb{R}$. Since u and v are parameters in (13), they remain constant along any shocks in the TWSs of (1)–(2) with $\varepsilon=0$.

The equilibria of (13) form a two-dimensional surface in (u,v,p,w)-space, referred to as the *critical manifold*, which can be represented as a graph over the original variables (u,w):

$$S:=\left\{(u,v,p,w)\;\middle|\; v=\left(c-\frac{u^2w}{c}\right)w,\quad p=\frac{u^2w}{c}\right\}. \tag{14}$$

The left-hand panel of Fig. 4 shows a projection of S into (u,v,w)-space.

Lemma 3.2. *The critical manifold S is folded around the so-called fold curve,*

$$F:=\{(u,w)\mid 2u^2w-c^2=0\}. \tag{15}$$

In other words, at F, two branches of equilibria $(p_\pm(u,v;c),w_\pm(u,v;c))$ of (13) originate in a saddle-node bifurcation, see for example Kuznetsov (2004) for the conditions of a saddle-node bifurcation. The equilibria $(p_-(u,v),w_-(u,v))$ are unstable, or repelling, with respect to (13) and, hence, we label this branch of S as S_r. The other branch of S, given by $(p_+(u,v;c),w_+(u,v;c))$, is stable, or attracting, and is labelled S_a. S is symmetric in w around F with $w_-\ge w_+$.

Proof. The proof follows from Wechselberger and Pettet (2010), and is similar to the proof of Lemma 2.2 in Harley et al. (2014a); we refer to these works for the details. Briefly: the folded structure of S follows from checking that the standard conditions for a saddle-node (SN) bifurcation are met (e.g. Kuznetsov, 2004); the stability of S is evident from the eigenvalue structure of the

linearisation of (13); and, the symmetry is a consequence of the definition of S.□

The folded structure of S allows heteroclinic connections between S_r and S_a. Such a connection transports a point (u_-, v_-, p_-, w_-) on S_r to the point (u_+, v_+, p_+, w_+) on S_a, with $u_+ = u_-$ and $v_+ = v_-$ (since u and v are constant in (13)), and

$$p_+ = \frac{u_-^2 w_+}{c} = c - p_-,$$
$$w_+ = \frac{c^2}{u_-^2} - w_- = 2F(u_-) - w_-. \tag{16}$$

These conditions follow from the definition of S and are equivalent to the Rankine–Hugoniot and Lax entropy conditions for shocks for the strictly hyperbolic system (1)–(2) with $\varepsilon = 0$; see Harley et al. (2014a); Marchant et al. (2000); Wechselberger and Pettet (2010). The second equation in (16) highlights the symmetry of S around F. The right-hand panel of Fig. 4 provides a schematic of S and an example heteroclinic connection between S_r and S_a via the dynamics of (13).

3.3. Reduced problem

On the slow scale, taking the singular limit of (11) yields a differential–algebraic system with two ODEs coupled to two algebraic constraints, termed the *reduced problem*:

$$\begin{aligned} u_z &= p, \\ v_z &= -w(1-w)(w-\alpha), \\ 0 &= \frac{1}{\beta}(u^2 w - cp), \\ 0 &= v + (p-c)w. \end{aligned} \tag{17}$$

As expected from geometric singular perturbation theory, the algebraic constraints define S. Herein lies the geometric structure of the model. When viewed on the slow scale, the flow along S is evident and governed by (17).

Since S is given as a graph over the original model variables (u, w), we restrict our investigation of (17) to these coordinates, where the slow behaviour is governed by

$$\begin{aligned} u_z &= \frac{u^2 w}{c}\left(c - \frac{2u^2 w}{c}\right), \\ w_z &= -w(1-w)(w-\alpha) + \frac{2u^3 w^3}{c^2}. \end{aligned} \tag{18}$$

Consequently, the analysis of the reduced dynamics reduces to a two-dimensional, (u,w)-phase plane analysis. In this projection, the phase space consists of two distinct regions corresponding to S_a and S_r, separated by F; see, for example, Fig. 8.

The equilibria of (18) in the first quadrant are

$$(u_\infty, 0), \quad (0, \alpha), \quad (0, 1), \quad u_\infty \in \mathbb{R}^+.$$

The stability of these equilibria is determined via the associated Jacobian matrix, appended with a perturbation analysis in the case of a zero eigenvalue:

- $(u_\infty, 0)$ has an unstable eigenvalue and a zero eigenvalue (related to the translation in the u direction);
- $(0, \alpha)$ has a stable eigenvalue with eigenvector pointing in the direction of the invariant w-axis and centre-unstable outgoing trajectories, directed into the first quadrant; and,
- $(0, 1)$ has an unstable eigenvalue with eigenvector pointing in the direction of the invariant w-axis and centre-unstable outgoing trajectories, directed into the first quadrant.

System (18) is singular along F, because the left-hand side of the w-equation vanishes here. In general, solution trajectories approaching F have w-derivatives that blow-up in finite time. The isolated points on F at which the right-hand side of (18) also vanishes, referred to as *canard points* (Benoit et al., 1981; Wechselberger, 2012), form the exception to this rule.

To understand solution trajectories of (18) interacting with these canard points, we introduce a new variable $\bar{z}$, defined via

$$\frac{\mathrm{d}z}{\mathrm{d}\bar{z}} = c - \frac{2u^2 w}{c}.$$

With this change of coordinate system, (18) transforms to the so-called *desingularised system*

$$\begin{aligned} \frac{\mathrm{d}u}{\mathrm{d}\bar{z}} &= \frac{u^2 w}{c}\left(c - \frac{2u^2 w}{c}\right), \\ \frac{\mathrm{d}w}{\mathrm{d}\bar{z}} &= -w(1-w)(w-\alpha) + \frac{2u^3 w^3}{c^2}. \end{aligned} \tag{19}$$

This system is more amenable to analysis than (18) as it is no longer singular. Canard points of (18) correspond to equilibria of (19) on F. They are classified according to the nature of the corresponding equilibrium in (19). For example, if (19) has a saddle equilibrium on F, then the corresponding canard point of (18) is called a *folded saddle canard point* (FS). Similarly, we have *folded focus canard points* (FF), *folded node canard points* (FN), *etc.* Two trajectories of a system with a FS can pass through F at such a canard point, thereby flowing from S_a to S_r and *vice versa* (Wechselberger, 2012). The former trajectory is labelled the *canard solution* and the latter the *faux canard solution*. Trajectories are not able to pass through F at a FF, while a *funnel* of trajectories pass through F at a FN (Wechselberger, 2005, 2012). Fig. 5 provides a

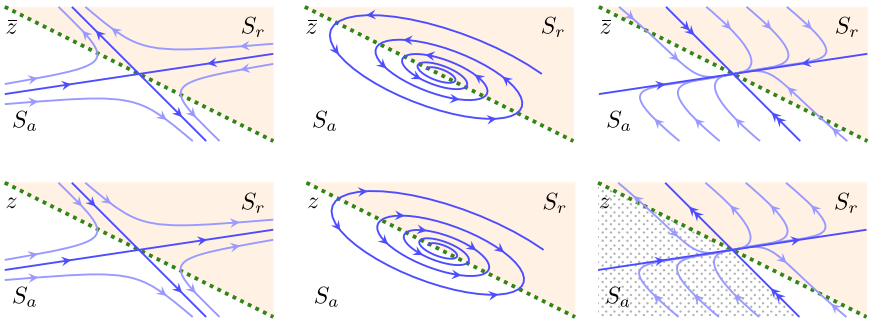

Fig. 5. Schematics of some types of canard points. The green dotted line represents F, the upper-right, shaded region S_r and the lower-left, unshaded region S_a. The upper panels show standard equilibrium points (saddle, focus, node), which lend their names to the corresponding canard points shown in the lower panels (folded saddle, folded focus, folded node). The difference between the upper and lower panels is the direction of the trajectories on S_r due to the parameterisation, $\bar{z}$ or z. A folded saddle admits two trajectories through it, along the stable and unstable manifolds of the corresponding saddle. A folded focus does not admit any trajectories. A folded node admits a *funnel* (dotted region) of trajectories between the stronger stable (or unstable) manifold of the corresponding node and F, which follow the weaker stable (or unstable) manifold. This is an adaptation of Fig. 10 in Harley et al. (2014b). (For interpretation of the references to color in this figure caption, the reader is referred to the web version of this paper.)

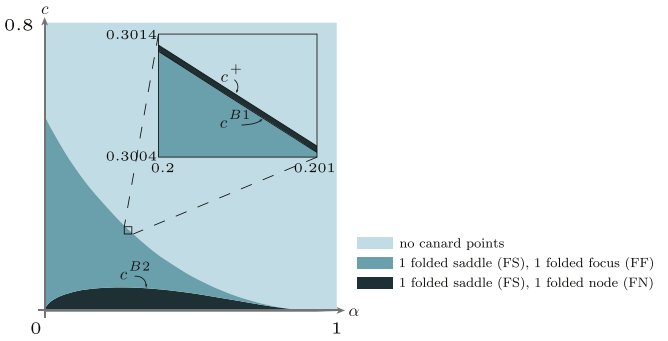

Fig. 6. The type of canard points of (18), in the (α, c)-plane. The canard points are created in a saddle-node bifurcation as c decreases through $c = c^+(\alpha)$, defined in (20). The folded node becomes a folded focus at $c = c^{B1}(\alpha)$ and a folded node once again at $c = c^{B2}(\alpha) < c^{B1}(\alpha)$. (For interpretation of the references to color in this figure caption, the reader is referred to the web version of this paper.)

schematic of a FS, FF and FN and illustrates their connection with regular equilibria.

Remark 3. The flows of (18) and (19) differ only in their parametrisation. The flows are topologically equivalent in forward $\bar{z}$ if $dz/d\bar{z} > 0$ and topologically equivalent in backward $\bar{z}$ if $dz/d\bar{z} < 0$. It is straightforward to see that $dz/d\bar{z} = c^2 - 2u^2 w < 0$ on S_r, or above F in the (u,w)-plane, while $dz/d\bar{z} = c^2 - 2u^2 w > 0$ on S_a, or below F in the (u,w)-plane. Thus, the (u,w)-phase plane of (18) is obtained from the (u,w)-phase plane of (19) by reversing the direction of the trajectories on S_r, or above F in the (u,w)-plane; see Fig. 8 for an illustration.

Lemma 3.3. *For $0 < \alpha < 1$, (18) has two canard points if $0 < c < c^+(\alpha)$, and no canard points otherwise, where*

$$c^+ = c^+(w^+(\alpha), \alpha) := 2\sqrt{2w^+}(1 - 2w^+ + \alpha) \tag{20}$$

and

$$w^+ = w^+(\alpha) := \frac{1}{6}\left(1 + \alpha + \sqrt{(1+\alpha)^2 + 12\alpha}\right).$$

The w-components of both canard points are larger than α and smaller than 1.

Proof. Canard points of (18) correspond to equilibria of (19) on F. The w-component of these equilibria is real positive roots of

$$q(w) := \sqrt{2}(1-w)(w-\alpha) = c\sqrt{w} =: s(w), \tag{21}$$

and the corresponding u-components are given by $u = c/\sqrt{2w}$. The number of solutions to (21) changes in a saddle-node (SN) bifurcation as $q(w)$ and $s(w)$ become tangent, which occurs at $c = c^+(\alpha)$. From the shapes of the graphs of $q(w)$ and $s(w)$ (parabolic and monotonically increasing, respectively) for different values of c, it follows that the smaller root of (21) lies between α and $w^+(\alpha)$, while the larger root lies between $w^+(\alpha)$ and 1. As $c \to 0$, the roots approach α and 1, and as $c \to c^+(\alpha)$, they approach $w^+(\alpha)$.□

We determine the type of the canard points by numerically computing the eigenvalues of the corresponding equilibria of (19). Since the canard points are created in a SN bifurcation, we observe a folded saddle (FS) and a folded node (FN) near the bifurcation point, $c = c^+(\alpha)$. Just after the SN bifurcation, at $c = c^{B1}(\alpha) < c^+(\alpha)$, the FN becomes a FF (while the FS remains a FS). The FF transitions back to a FN at $c = c^{B2}(\alpha) < c^{B1}(\alpha)$; see Fig. 6. While $c^+(\alpha)$ is determined analytically, and defined in (20), $c^{B1,B2}(\alpha)$ are determined numerically.[5]

[5] In principle, it may be possible to determine $c^{B1,B2}$ analytically: the canard points correspond to roots of (21) and these roots are a subset of the roots of a quartic polynomial. However, these expressions are so complicated they offer little insight.

Lemma 3.4. *For $0 < \alpha < 1$ and $0 < c < c^+(\alpha)$, with $c^+(\alpha)$ defined in (20), (18) admits a solution trajectory connecting $(0,1)$ to the FS.*

Proof. For $0 < \alpha < 1$ and $0 < c < c^+(\alpha)$, Lemma 3.3 implies that (18) has two canard points, (u_{FS}, w_{FS}) and (u_F, w_F), with $\alpha < w_F$, $w_{FS} < 1$. It is straightforward to show that the FS, (u_{FS}, w_{FS}), is the canard point with the larger w-component. Since F corresponds to a monotonically decreasing function of w as u increases, $u_{FS} < u_F$. Consequently, (u_{FS}, w_{FS}) lies above and to the left of (u_F, w_F) in the (u,w)-phase plane. From (18) it follows that $u' > 0$ for $w, c > 0$ and that $w' < 0$ along $w = w_F$ for $0 < u < u_F$. Consequently, the trajectory leaving $(0, \alpha)$ does not connect to (u_{FS}, w_{FS}). Since the u-axis is repelling, it intersects F below and to the right of (u_F, w_F). The w-nullcline connecting $(0,1)$ with the FS is strictly decreasing and the stable eigenvector of the FS lies below that nullcline for $u \lessapprox u_{FS}$. As a result, there is a trajectory leaving $(0,1)$ that connects to (u_{FS}, w_{FS}).□

This solution trajectory (that leaves $(0,1)$, connects to (u_{FS}, w_{FS}) and, hence, continues onto S_r) is the canard solution, which we label T_o. It is the only solution trajectory of (18) that (partly) lives on S_r and connects to $(0,1)$.

In the remainder of this paper, we do not consider regimes where FNs are present: $0 < c < c^{B2}$ and $c^{B1} < c < c^+$. Although we suspect that our results are valid for $0 < c < c^+$, the analysis of FNs is beyond the scope of this paper.

Remark 4. In the case $\beta = 0$, the u-equation of (9) is of first order. In this case, u_z is simply $\frac{u^2 w}{c}$ and the singularly perturbed system becomes three-dimensional.

$$\begin{aligned} u_z &= \frac{u^2 w}{c}, \\ v_z &= -w(1-w)(w-\alpha), \\ \varepsilon w_z &= v - cw + \frac{u^2 w^2}{c}. \end{aligned} \tag{22}$$

Consequently, the layer problem becomes one-dimensional, but the definition of S and the symmetry it has around the fold curve F remain unchanged. Hence, the reduced system and the slow behaviour are independent of β, and for $\beta = 0$ are described by (18). This is also supported by the simulations of the full PDE system with $\beta = 0$, see Fig. 7 which has identical parameter values as Fig. 2, besides $\beta = 0$. The case $\beta = 0$ applies to tumours of which the dominant mechanism of cell migration is haptotaxis rather than chemotaxis, like some solid tumours.

3.4. Proof of Theorem 3.1

Travelling wave solutions (TWSs) are identified in the four-dimensional phase space of (11) or (12) as heteroclinic connections between the equilibria

$$(u, v, p, w) = (0, c, 0, 1) \quad \text{and} \quad (u, v, p, w) = (u_\infty, 0, 0, 0).$$

To leading order, flow in the four-dimensional phase-space can be represented by concatenations of the fast flow of (13) with u, v constant, describing the TWSs around the shock, and the slow flow of (17), describing the TWSs away from the shock. This *glueing together* of solution segments from (13) and (17) is how we construct leading order approximations of TWSs of (1)–(2). The validation of this approach follows from GSPT and canard theory.

Since both equilibria lie on S_a, they both have two-dimensional stable manifolds in (13) and a two-dimensional centre manifold corresponding to the slow variables. Consequently, a heteroclinic connection cannot be made between the two equilibria purely within (13). Similarly, since $(u_\infty, 0)$ in (18) has a one-dimensional unstable manifold (since $\alpha > 0$) and a one-dimensional centre manifold corresponding to translation in the u-direction, a heteroclinic connection cannot be made between the two equilibria

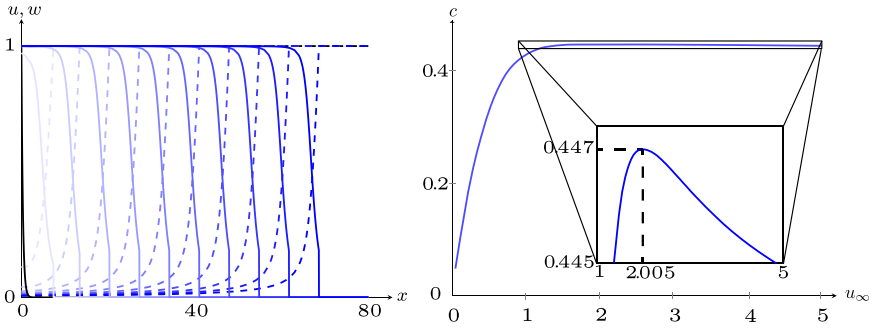

Fig. 7. Left-hand panel: A *Type III wave* with a biologically justified, well-defined edge and speed $c \approx 0.43$, obtained by numerically simulating (1)–(2) with $\varepsilon = 0.001$, $\alpha = 0.05$ and $\beta = 0$. The dashed lines correspond to u-profiles and the solid lines to w-profiles, with solutions plotted at $t = 0$ (black), 16 (lightest), 32,…, 160 (darkest). Note that this is very similar to the left panel of Fig. 2, because only the fast dynamics is influenced by β, see (13). Right-hand panel: The leading order ($\varepsilon = 0$) component of the speed of travelling wave solutions of (1)–(2) (c) versus the background ECM density (u_∞), with $\alpha = 0.05$, illustrating a biphasic relationship. This is exactly the same as the right-hand panel of Fig. 2 as the leading order component is independent of β, see (18).

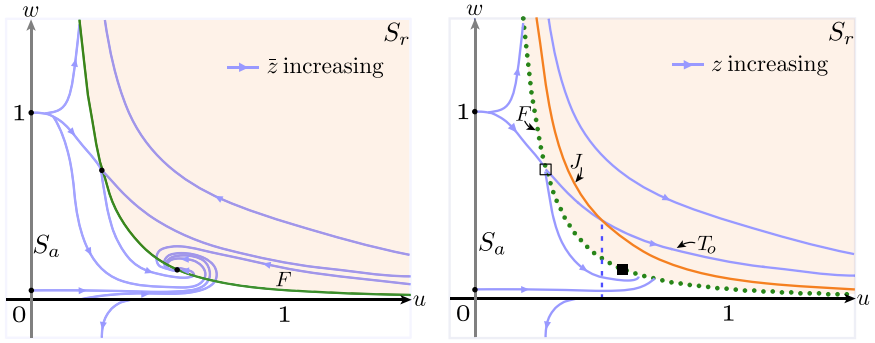

Fig. 8. Phase planes of (19) (left) and (18) (right), for $\alpha = 0.05$ and $c = 0.33$. The green line is the fold curve (F), which is dotted on the right to illustrate its singularity. Black dots represent equilibria. The black open square is a folded saddle and the solid black square is a folded focus. F divides S into a repelling side (S_r, shaded) and an attracting side (S_a, not shaded). The canard solution is labelled T_o (take-off). The curve J given by $w = J(u) = c^2/u^2$ and is a reflection of the u-axis in F. An intersection between J and T_o determines the u_∞ for which a Type III travelling wave solution (with speed c) exists. Here, only one intersection exists. (For interpretation of the references to color in this figure caption, the reader is referred to the web version of this paper.)

purely within (18). Instead, a connection must contain solution segments from both systems. Consequently, no TWSs exist when no canard points are present ($c > c^+(\alpha)$) and TWSs of (1)–(2) can only be Type III waves since the final part of the heteroclinic connection for $\varepsilon = 0$ has to be a trajectory of (13).

According to Lemma 3.2 and (16), the fast flow is directed from S_r to S_a and the w-component is symmetric in F, while the u-component is constant. Hence, a heteroclinic connection to $(u_\infty, 0, 0, 0)$ on S_a via (13) must *take-off* from $(u_\infty, 0, 0, c^2/u_\infty^2)$ on S_r. The canard solution is the only solution of the slow flow that (partly) lives on S_r and that connects to S_a in backward z. So, to construct a heteroclinic connection between $(0, c, 0, 1)$ and $(u_\infty, 0, 0, 0)$, we need the canard solution (in four-dimensional space) to intersect $(u_\infty, 0, 0, c^2/u_\infty^2)$. In the original, (u, w)-coordinates, this means that the canard solution of (18) (T_o) must intersect the *jump curve*: $J := c^2/u_\infty^2$. In Fig. 8, the phase plane of (18) and J are shown for particular values of α and c; T_o and J intersect, yielding a heteroclinic connection of (9) and (10) with $\varepsilon = 0$ and, hence, a Type III TWS of (1)–(2) with $\varepsilon = 0$.

With $\varepsilon > 0$, the end states $(0, 1)$ and $(u_\infty, 0)$ do not perturb. Geometric singular perturbation theory implies that the (invariant) manifolds S_a and S_r perturb to the $\mathcal{O}(\varepsilon)$-close, locally invariant manifolds $S_{a,\varepsilon}$ and $S_{r,\varepsilon}$, respectively, provided S_a and S_r are normally hyperbolic and ε is sufficiently small. Along F, S loses normal hyperbolicity. However, canard theory guarantees that T_o persists (Wechselberger and Pettet, 2010).

If the unstable manifold of $(0, 1)$ and the stable manifold of $(u_\infty, 0)$ have a transverse intersection for $\varepsilon = 0$, the heteroclinic connection for $\varepsilon = 0$ persists as a solution of (9)–(10) with $0 < \varepsilon \ll 1$. This condition is equivalent to J and T_o intersecting transversally. In Appendix D, we show that this *transversality condition* holds, provided $c \neq u_\infty \sqrt{\alpha}$. Hence, a TWS that is constructed for $\varepsilon = 0$, persists as a TWS of (1)–(2), with $0 < \varepsilon \ll 1$ sufficiently small, provided $c \neq u_\infty \sqrt{\alpha}$, with the former providing a leading order approximation of the latter.

4. Implications of the strong Allee effect

In the previous section, we introduced the mathematical framework to study invasive tumour fronts, or travelling wave solutions (TWSs), of the strong Allee model (1)–(2) (with $0 \lessapprox \alpha < 1$, $0 \leq \beta \leq 1$ and $0 \leq \varepsilon \ll 1$ sufficiently small) connecting the all-cancer state $(0, 1)$ and the cancer-free state $(u_\infty, 0)$ with $u_\infty \in \mathbb{R}^+$. It was shown, in a mathematically rigorous way, that the strong Allee model cannot admit Type I, II or VI TWSs (see Theorem 3.1); only TWSs where the w-component has a well-defined edge—Type III waves—can exist. This result is due to the stability of the states $(u_\infty, 0)$. While Type III waves are the only possible TWSs of the strong Allee model, their existence is not guaranteed. In Section 3, we derived a condition for the existence of Type III waves.

In this section, we establish the main results presented in Section 1.3.1. We demonstrate the existence of Type III TWSs in the strong Allee model and investigate the relationship between their speed and the background ECM density (u_∞), for different values of ε. We also make a qualitative comparison between the results for the strong Allee model and results for the logistic model, (1) with (3), (Harley et al., 2014a) and the competition model, (1) with (4), (Marchant et al., 2006), and review the impact of the inclusion of the strong Allee effect.

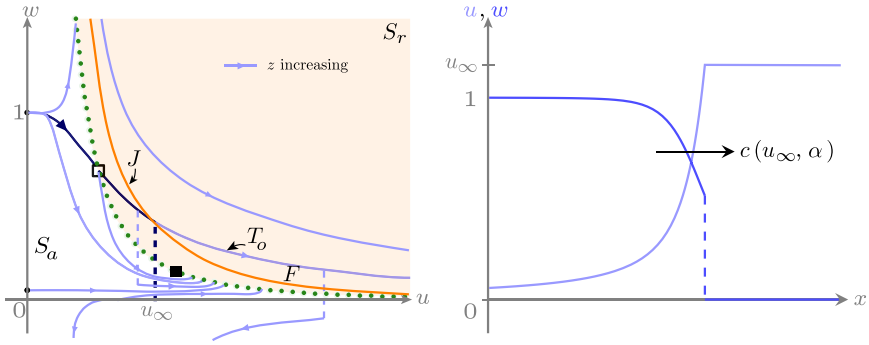

Fig. 9. Left-hand panel: An example phase plane of (23), with $\alpha = 0.05$ and $c = 0.33$. The green dotted line represents the fold curve, labelled F, and the open black square represents the folded saddle, at which the canard solution, labelled T_o, crosses the fold curve. The solid blue lines correspond to trajectories of (23) and the dashed blue lines correspond to shocks. The jump curve, labelled $J := c^2/u^2$, is shown in orange. A Type III travelling wave solution of the strong Allee model exists since the jump curve and the canard solution intersect transversally. The solid black square is a folded focus canard point, which does not play a role in the construction of travelling wave solutions. Right-hand panel: An illustration of the Type III travelling wave solution (as a function of x) that is obtained from the dark blue trajectory in the phase plane. The w-component has semi-compact support and $u_\infty > 1$ is chosen arbitrarily. (For interpretation of the references to color in this figure caption, the reader is referred to the web version of this paper.)

4.1. Existence of invasive tumour fronts with well-defined edges

Type III TWSs of the strong Allee model exist if a transverse intersection between two specific curves in the phase plane of the ODE system

$$u_z = \frac{u^2 w}{c},$$
$$\left(c - \frac{2u^2 w}{c}\right) w_z = -w(1-w)(w-\alpha) + \frac{2u^3 w^3}{c^2} \tag{23}$$

exists; see Section 3 for the derivation of this condition. The two curves are the so-called *canard solution*, denoted T_o in Fig. 9, and the so-called *jump curve*, denoted $J := c^2/u^2$ in Fig. 9. Here, u and w still represent the ECM and cancer cell densities, c is the invasion speed of the tumour and $z = x - ct$ is a new variable—the so-called *travelling wave coordinate*—that corresponds to a coordinate frame moving along with the TWS. Note that (23) can also be obtained from the strong Allee model by setting $\varepsilon = 0$ and looking for stationary solutions in the z-coordinate frame.

A consequence of the requirement of an intersection between the canard solution and the jump curve is that no TWSs exist for c greater than a critical value, $c = c^+(\alpha)$, defined in (20), as the canard solution does not exist in this regime; see Section 3. The behaviour of c^+ as a function of α is shown as the transition curve between the light and dark green regions in Fig. 6, which shows that $c^+(\alpha)$ is a decreasing function of the Allee threshold α. Tumours requiring a larger threshold to grow, therefore have a slower maximum speed potential. Henceforth, we only consider speeds $c^{B2}(\alpha) < c < c^{B1}(\alpha) < c^+(\alpha)$, where $0 < c \le c^{B2}(\alpha)$ and $c^{B1}(\alpha) \le c < c^+(\alpha)$ are narrow regions where the mathematical analysis becomes more involved and is beyond the scope of this paper. The analytic expression $c^+(\alpha)$ hence yields an upper bound on the speed of the invading waves. Consequently, the model does not support travelling waves that go faster than this upper limit. So, the expression $c^+(\alpha)$ can be used as a crude measure to give an upper bound on how far an invading wave has travelled at any time without any significant computation. Because $c^+(\alpha)$ is decreasing, a larger α gives a lower upper bound on the speed.

With $c^{B2}(\alpha) < c < c^{B1}(\alpha)$, the canard solution is the only solution trajectory of (23) that leaves the all-cancer state $(0, 1)$ and crosses the so-called *fold curve*, denoted $F := c^2/2u^2$ in Fig. 9. (This fold is a projection in two dimensions of the fold F of the critical manifold as shown in Fig. 4). Other trajectories leaving $(0, 1)$ also hit the fold curve, but do not cross it due to the singular nature of (23); at the point where the canard solution crosses the fold curve both the left- and right-hand sides of the second equation in (23) vanish. This point is a *folded saddle canard point* (FS).

A TWS of the strong Allee model corresponds (to leading order in ε) to the canard solution until it intersects the jump curve, at say $(u, w) = (u_*, c^2/u_*^2)$, at which point it jumps to $(u_\infty, 0)$. This jump corresponds to a shock in the w-component of the (leading order) TWS that connects to zero, while the u-component stays constant ($u = u_*$), creating a Type III TWS with cancer-free state $(u_\infty, 0) = (u_*, 0)$ and speed c (to leading order); see Fig. 9. The length of the shock is c^2/u_*^2, which is double the distance between the u-axis and the fold curve at $u = u_*$. In other words, the jump curve is the reflection of the u-axis around the fold curve.

Fig. 9 provides an example phase plane of (23) for given α and c, and a schematic of the Type III TWS that the strong Allee model admits for this parameter set. The fold curve is indicated by the green dotted line. The solid blue lines are solution trajectories of (23) and the unique solution trajectory crossing the fold curve (the canard solution) is labelled T_o. Potential shocks are indicated by the dashed blue lines. Due to the symmetry of the shock, the length of the dashed blue lines is twice the distance between the canard solution and the fold curve and the given u-coordinate. Since $(u_\infty, 0)$ are repelling equilibrium points of (23), trajectories of (23) cannot connect to the u-axis as $z \to \infty$. Consequently, only shocks landing exactly on the u-axis create TWSs; such TWSs are Type III TWSs. The connection to the u-axis occurs if and only if $u_* = u_\infty$; only if the canard solution intersects the jump curve is a Type III TWS created. The jump curve is indicated by the orange curve in Fig. 9. For the given parameters, there is a unique intersection between the canard solutions and the jump curve. Therefore, with $\alpha = 0.5$, the strong Allee model admits a unique Type III TWS that travels with speed $c = 0.33$ and asymptotes to the cancer-free state $(u_\infty, 0) = (u_*, 0)$ (to leading order).

4.2. Biphasic relationship between invasion speed and background ECM density

In the previous section, we discussed how Type III travelling wave solutions (TWSs) are created. However, several questions remain:

1. For a given α and c, does an intersection between the canard solution and the jump curve always exist, such that a Type III TWS is created?
2. If such an intersection exists, is it unique?
3. Can different speeds yield TWSs that asymptote to the same cancer-free state $(u_\infty, 0)$ with α fixed?

The first question is answered in Section 3 and discussed in the previous section. For $c > c^+(\alpha)$, there is no canard solution and, thus, no TWSs exist. However, neither Section 3 nor the previous section guarantee that the required intersection exists for $c^{B2}(\alpha) < c < c^{B1}(\alpha) < c^+(\alpha)$, despite the canard solution existing in this regime.

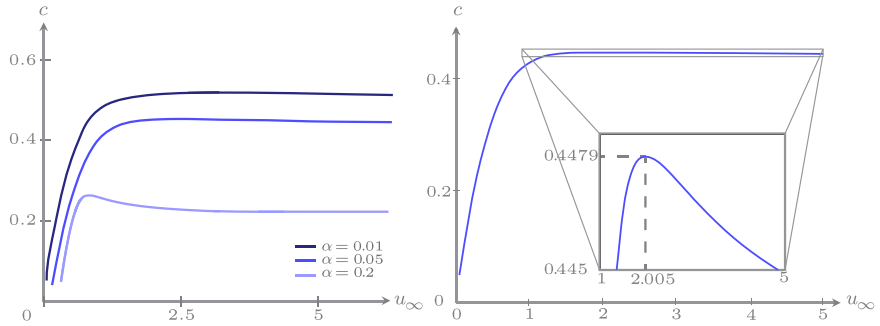

Fig. 10. Left-hand panel: The leading order speed of the invasive tumour fronts as a function of the background ECM density, for $\alpha = 0.01, 0.05, 0.2$. For increasing α, the *biphasic relationship* between c and u_∞ becomes more prominent and the wavespeed for a given u_∞ decreases. Right-hand panel: A close-up of the $\alpha = 0.05$-curve in the left-hand panel, highlighting that the biphasic relationship.

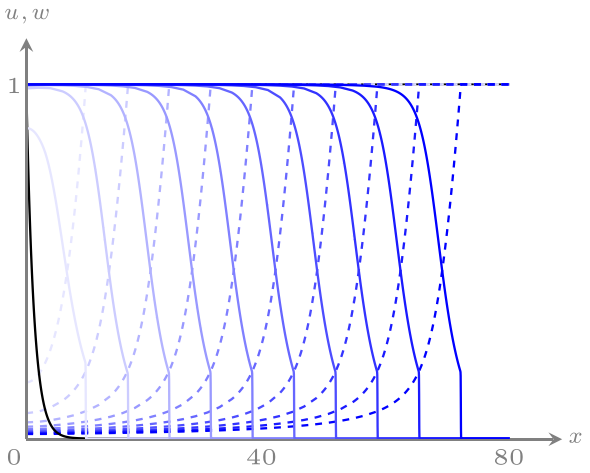

Fig. 11. A numerical simulation of (1)–(2), with $\alpha = 0.05$, $\beta = 0.5$, $\varepsilon = 0.001$, $u_\infty = 1$ and a measured speed $c \approx 0.43$, consistent with the ODE results. The dashed lines correspond to u-profiles and the solid lines to w-profiles, with solutions plotted at $t = 0$ (black), 16 (lightest), 32,…, 160 (darkest).

An investigation of the phase portraits of (23) for different values of α and c provides further insight into this, and the other questions. The results are presented in Fig. 10, where the (leading order) speed of the Type III TWS c (if such a TWS exists) is indicated, for the chosen values of α and u_∞.

Fig. 10 suggests that there is an upper limit $c = c^{\text{trans}}(\alpha)$ on the values of c for which there exists an intersection between the canard solution and the jump curve. This upper limit appears to be less than $c^{\text{B1}} < c^{+}(\alpha)$ and satisfies the transversality condition derived in Appendix D. Consequently, the corresponding value of $u_\infty = u_\infty^{\text{trans}}$ is related to c^{trans} via $c^{\text{trans}} = \sqrt{\alpha} u_\infty^{\text{trans}}$. Moreover, for fixed α, different values of c yield different u_∞-values and it appears that TWSs to all cancer-free states $(u_\infty, 0)$ can be constructed. For a given α, the relationship between the invasion speed of the tumour (c) and the background ECM density (u_∞) has a single turning point—a maximum—at $u_\infty = u_\infty^{\text{trans}}(\alpha)$ with speed $c^{\text{trans}} = \sqrt{\alpha} u_\infty^{\text{trans}}$. This *biphasic* relationship qualitatively resembles experimental results for malignant tumour invasion reported in Perumpanani and Byrne (1999), where the relationship between the collagen concentration and invasion distance of HT1080 is measured to be non-monotonic. Moreover, the non-monotonicity becomes more pronounced as α increases. Consequently, there is no intersection between the canard solution and the jump curve for $c > c^{\text{trans}}$, and, therefore, no TWS. For $c < c^{\text{trans}}$ there is a narrow region where two intersections exist, which implies the existence of two TWSs, with different end states, that travel with identical speed. However, since the relationship between u_∞ and c illustrated in Fig. 10 is a graph over u_∞, each background state $(u_\infty, 0)$ corresponds to a single invasion speed. Hence, for a given α and u_∞, we obtain a unique TWS. Fig. 10 indicates that for increasing α and for fixed u_∞, this speed decreases.

4.3. ODE versus PDE

The phase plane and wave shape illustrated in Fig. 9 as well as the wave-speed results presented in Fig. 10 are for the strong Allee model with $\varepsilon = 0$. However, provided we are not near the turning point of the biphasic relationship, where transversality between the canard solution and the jump curve is lost, the shape and speed of these travelling wave solutions (TWSs) are good approximations of TWSs of strong Allee model with $0 < \varepsilon \ll 1$; see Section 3.4. It is probable that even near the turning points, the $\varepsilon = 0$-solutions are good approximations of the $\varepsilon > 0$-solutions. The location of the turning point will simply shift. However, further mathematical analysis is required to confirm this.

Fig. 11 provides an example simulation of (1), the strong Allee model with $\varepsilon > 0$, away from the turning point. This simulation shows the evolution of a Type III wave with a speed that agrees with that predicted by the phase plane analysis, up to $\mathcal{O}(\varepsilon)$-corrections. The figure also suggests that the invasive tumour front is stable, in the sense that it is observable in the system. The initial conditions for this particular simulation are $(u, w) = (u_\infty, e^{-x})$. However, the same invasive tumour front, with the same speed, appears to evolve from any exponentially decaying w-initial condition, or a w-initial condition with semi-compact support.

Fig. 12 depicts the results of further numerical simulations for a range of ε and u_∞ values, $\alpha = 0.05$ and $\beta = 0.5$; the right-hand panel is a close-up of the left-hand panel. The solid curve is the biphasic relationship for $\varepsilon = 0$ and $\alpha = 0.05$, given in Fig. 10. The markers indicate the measured speed of the Type III TWS that evolves from the numerical simulation of strong Allee model, with $\varepsilon > 0$ as indicated. These results demonstrate that for a given u_∞ and α, the invasion speed is an $\mathcal{O}(\varepsilon)$ perturbation of the $\varepsilon = 0$-speed, as expected; see Section 3.4. Moreover, they suggest that near the maximum of the solid curve, Type III TWSs continue to exist for $\varepsilon > 0$ with speeds close to the $\varepsilon = 0$-speed. This observation supports our previous claim that while the mathematical analysis breaks down near the maximum, the results are not significantly altered.

The light blue dashed and dotted curves in Fig. 12 are values of c at which the phase plane of (23) changes qualitatively, for $\alpha = 0.05$; see Fig. 6. For c-values between these lines, the folded focus canard point (FF) denoted by the filled black square in Fig. 9, remains a FF. The values of c between the light blue dashed and dotted curves $(c^{\text{B2}}(\alpha) < c < c^{\text{B1}}(\alpha))$ represent the regime analysed mathematically in Section 3.

Thus, we require that for a given α, u_∞ is chosen in such a way that the resulting TWS has a speed in this regime. Based on Fig. 12, for $\alpha = 0.05$, the minimum value of u_∞ appears to be less than 0.05 (the smallest value we tested). Since $c^{\text{trans}} < c^{\text{B1}}$, there does not

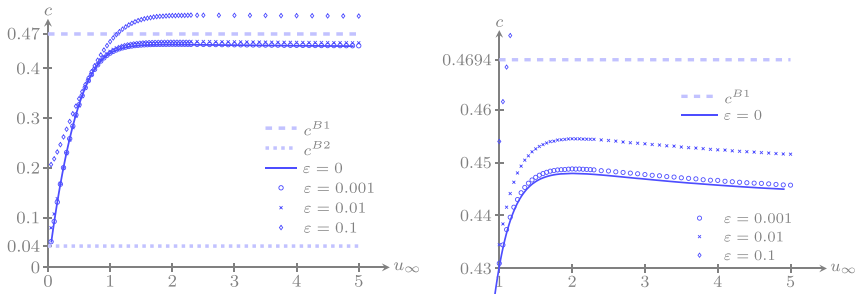

Fig. 12. The relationship between u_∞ and the measured speed c for Type III travelling wave solutions obtained by numerically simulating (1)–(2) with $\alpha = 0.05$, $\beta = 0.5$ and ε as indicated, together with bifurcation values of c for $\alpha = 0.05$; see Section 3.3. The solid curve indicates the relationship between u_∞ and c for Type III travelling wave solutions with $\alpha = 0.05$ and $\varepsilon = 0$, given in Fig. 10. The right-hand panel is a close-up of the left-hand panel. The biphasic relationship is clearly visible for small ε.

appear to be an upper bound on u_∞. The $c^{B1,B2}$ lines will perturb for $\varepsilon > 0$, which may affect the range of appropriate choices of u_∞. However, the appearance of qualitatively similar TWSs of the strong Allee model for a range of ε values suggests that our analysis remains valid for reasonably large ε-values (say, $\varepsilon = 0.1$).

4.4. Comparison with models with logistic growth

In this section, we make a qualitative comparison between the strong Allee model and the logistic ((1) with (3)) and competition ((1) with (4)) models. The logistic model, where cancer cell growth is modelled by a logistic growth term, is studied extensively in Harley et al. (2014a). The competition model, where a term representing the competition for space between the ECM and cancer cells is appended to a logistic growth term, is studied in Marchant et al. (2006). The results of the previous sections, for the strong Allee model, differ from those derived previously, in two main aspects.

For the logistic and competition models, there exists a range of travelling wave solutions (TWSs) with different speeds for a given background ECM density, varying from Type I–IV. This is in contrast to the unique TWS for the strong Allee model. Moreover, this unique TWS is of Type III, the most biologically relevant type, and appears to be stable in the sense that this kind of TWS is observed in numerical simulations of the PDE system, for a wide range of initial conditions. In contrast, for both the logistic and competition models all the Type I–III TWSs appear to be stable. See, for example, Fig. 1 in Harley et al. (2014a) where stable Type I–III TWSs are shown.

The biphasic relationship observed experimentally in malignant tumour invasion (Perumpanani et al., 1999), occurs in the competition model (Marchant et al., 2006, Fig. 10) but not in the logistic model. For the logistic model, the relationship between the invasion speed of the Type III waves and the background ECM density is monotonically increasing (Harley et al., 2014a, Fig. 11). Thus, we conclude that the relationship between u_∞ and c has changed qualitatively due to the Allee effect, in comparison with logistic growth.

5. Discussion and future work

In this paper, we proposed, what is to our knowledge, one of the first model of malignant tumour invasion that explicitly includes Allee effects. The analysis and results lead us to the conclusion that this model, with the strong Allee effect, is a better model of types of malignant tumour invasion in which hapto- or chemotaxis is the dominant mechanism of cell migration than similar, previously studied models: the logistic model (Perumpanani et al., 1999; Marchant et al., 2000; Harley et al., 2014a) and the competition model (Marchant et al., 2006). This conclusion is based on the strong Allee model's ability to replicate experimentally observed features of malignant tumour invasion more effectively than the previous models. In particular, the two main results that lead to this conclusion are:

1. The strong Allee model only admits Type III waves, the most biologically relevant invasive tumour fronts, rather than the whole family of Type I–IV waves that is admitted by the logistic and competition models.
2. The relationship between the invasion speed of these Type III waves and the background ECM density is biphasic, which is consistent with experimental observations, contrary to the corresponding relationship for the logistic model.

The results for the weak Allee model are less interesting; see Appendix B. They lead to the conclusion that the weak Allee model is similar to the logistic or competition models as a model of malignant tumour invasion. It admits the same family of travelling wave solutions, including those that are not biologically relevant, and does not exhibit the experimentally justified biphasic relationship between the speed of the Type III waves and the background ECM density.

5.1. Additional biological processes

The kinetic function for the cancer cells that we study is a general representation of a cubic function with zero constant term, negative cubic term and positive quadratic term:

$$f_{\text{Allee}}(\hat{w}) = -k_1\hat{w}^3 + k_1(k_2+k_6)\hat{w}^2 - k_1k_2k_6\hat{w} =: K_1\hat{w}^3 + K_2\hat{w}^2 + K_3\hat{w}, \tag{24}$$

with $K_1 < 0$ and $K_2 > 0$. Thus, appropriate modifications to the second equation in (6) (in the form of linear, quadratic or cubic terms in $\hat{w}$) can be expressed and studied using (1)–(2); the interpretation of the parameters simply changes. Consequently, the results of the Allee model apply more generally and we may use them to infer the effects of including (appropriate) additional biological processes to (6).

For example, the death of the cancer cells as a result of treatment or therapy can be modelled by the linear death term $-k_7\hat{w}$, with $k_7 > 0$ (s^{-1}). Appending this term to the $\hat{w}$-equation of (6) yields

$$\begin{aligned}\frac{\partial \hat{u}}{\partial \hat{t}} &= -k_4\hat{u}^2\hat{w} + D_1\frac{\partial^2\hat{u}}{\partial \hat{x}^2},\\ \frac{\partial \hat{w}}{\partial \hat{t}} &= k_1\hat{w}(k_2-\hat{w})(\hat{w}-k_6) - k_7\hat{w} - k_3\frac{\partial}{\partial \hat{x}}\left(\frac{\partial \hat{u}}{\partial \hat{x}}\hat{w}\right) + D_2\frac{\partial^2\hat{w}}{\partial \hat{x}^2}.\end{aligned} \tag{25}$$

Upon applying the nondimensionalisation

$$u_{\text{d}} = \frac{\hat{u}}{U_{\text{d}}}, \quad w_{\text{d}} = \frac{\hat{w}}{W_{\text{d}}}, \quad t_{\text{d}} = \frac{\hat{t}}{T_{\text{d}}}, \quad x_{\text{d}} = \frac{\hat{x}}{X_{\text{d}}}, \tag{26}$$

with

$$U_{\text{d}} = \frac{k_1}{k_4}W_{\text{d}}, \quad W_{\text{d}} = \frac{1}{2}\left(k_2+k_6+\sqrt{(k_2-k_6)^2 - 4\frac{k_7}{k_1}}\right),$$

$$T_{\text{d}} = \frac{1}{k_1W_{\text{d}}^2}, \quad X_{\text{d}} = \sqrt{\frac{k_3}{k_4W_{\text{d}}}},$$

and

$$\alpha_d := \frac{k_2+k_6}{W_d} - 1, \quad \beta_d := \frac{D_1}{D_2} = \beta, \quad \varepsilon_d := \frac{k_4}{k_1 k_3 W_d} D_2,$$

and dropping the subscript d, (25) transforms to the Allee model, (1)–(2). We assume $k_7 < k_7^* = k_1(k_2-k_6)^2/4$ so that W_d is real-valued.

To interpret the effect of the additional death term, we analyse how the dimensionless variables and parameters change between (7) and (26), keeping the remaining dimensional parameters k_i, $i \in \{1,2,\ldots,6\}$ fixed. The death rate k_7 appears directly in W_d and indirectly via W_d in the other terms (excluding $\beta_d = \beta$). It is straightforward to see that a death rate k_7 decreases W_d compared to W: $W_d < W$. Consequently,

$$U_d < U, \quad T_d > T, \quad X_d > X, \quad \alpha_d > \alpha, \quad \beta_d = \beta, \quad \varepsilon_d > \varepsilon.$$

As expected, the expression for W_d corresponds to the background state of (25) that represents the carrying capacity of the cancer cell density; the cancer cell density in (2) has been scaled to one so the *representative* cancer cell density $W_{[\cdot]}$ used in the nondimensionalisation must correspond to this background state. In terms of their relationship to W_d, the other quantities in the nondimensionalisation remain unchanged.

The parameter α_d represents the ratio of the two nontrivial w-background states of (25), consistent with α in (2). Consequently, for $\alpha_d > 0$, this parameter still imposes a growth threshold. However, in terms of the dimensional variables, the growth threshold is no longer represented by $k_6 > 0$ but by $k_6 + k_7/(k_1 k_2) > 0$. Increasing k_7 causes the two nontrivial $\hat{w}$-background states of (25) to approach each other on the $\hat{w}$-axis, until they collide and become complex-valued at $k_7 = k_7^*$. In (2), since the greater background state is scaled to one, increasing k_7 increases the value of the lesser nontrivial $\hat{w}$-background state, which has been scaled to α. Consequently, to obtain results for (25) we take $\alpha < \alpha_d < 1$ (with $\alpha_d \to 1$ as $k_7 \to k_7^*$). As evidenced by Fig. 10, for $\alpha > 0$, increasing α causes an overall decrease in the speed of the waves. Thus, adding a linear death term to the strong Allee model slows the invasive tumour fronts.

5.2. Shortcomings and future work

In this paper, we proposed a model of malignant tumour invasion that we argue is an improvement on previously studied models of its kind. However, our proposed model is still far from a complete description of malignant tumour invasion; any mathematical model describing a biological process is highly simplified. It is rarely possible to identify the exact mechanisms that are involved in a given process and parameter values such as reaction rates are often only known to several orders of magnitude. Even if the biology is completely understood, it remains a challenge to represent it mathematically in a way that is both accurate and manageable. For example, irregularities in the border of malignant tumours can be important (e.g. Amar et al., 2011), contributing to the speed and severity of the tumour. However, to capture these irregularities, two- or three-dimensional models must be used. Such models are highly complex and not conducive to rigorous mathematical analysis. In the quickly developing field of cancer research, the correct formulation of a model is an ongoing debate. We chose to model the Allee effect with the cubic function (2). However, other functional forms may also be used; see, for example, Courchamp et al. (2008) and references therein. Nevertheless, simple models, such as the Allee model, still provide useful information. In this case, we demonstrate that using the strong Allee effect instead of logistic growth has strong implications on the modelling of malignant tumour invasion. They also provide a stepping stone towards understanding more realistic, complex models.

The mathematical methods in this paper focus on proving the existence of travelling wave solutions. Although the PDE simulations provide an indication of which of these solutions are stable, a rigorous stability analysis remains to be undertaken. One method of inferring stability results for models such as (1) is based on an Evans function computation. Such a method is currently under development; see Harley et al. (2015). A related aspect that is not discussed in this paper is the *transient dynamics* of the travelling wave solutions. We do not discuss how an initially small, localised patch of cancer cells evolves into an invading tumour front or how the cancer cells come to be present in the first place. Instead, we investigate the possible long term behaviours of pre-existing tumours. An alternative model is necessary to describe the early stages of tumour development; the prime feature of the strong Allee effect is the growth threshold it imposes, which causes populations less than the threshold value to become extinct. The stability and transient dynamics of the traveling wave solutions studied here are topics for future research.

Finally, our analysis is only valid for sufficiently small values of ε. The numerical simulations suggest that our results remain (at least qualitatively) sound for quite large values of ε, say, $\varepsilon = 0.1$ (see, for example, Fig. 12). However, we purposely avoid specifically defining *sufficiently small* as this goes beyond the scope of this paper. An investigation of the effect of larger ε is left for future research.

Acknowledgements

LS gratefully acknowledges support from NDNS+ and thanks Queensland University of Technology for their hospitality. KH gratefully acknowledges support from an Australian Mathematical Society Lift-off Fellowship. PvH was supported under the Australian Research Council's Discovery Early Career Researcher Award funding scheme DE140100741. SB was supported by the Australian Research Council through Grant FT130100484.

Appendix A. Logistic growth and the Allee effect

To gain an understanding of the influence of the Allee effect, in comparison to logistic growth, consider the two ordinary differential

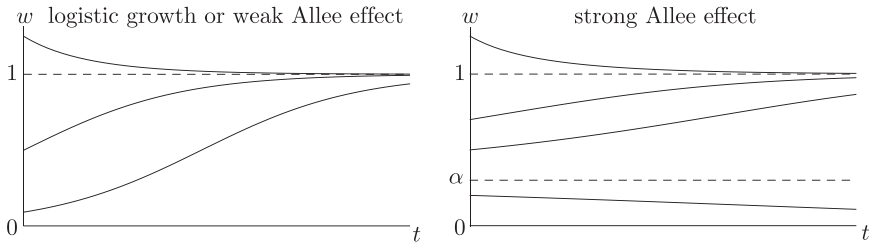

Fig. A1. Sketches of the solutions to the ODEs in (A.1). Left-hand panel: The ODEs with logistic growth and the weak Allee effect yield growth (or decay) to the carrying capacity (scaled to one) for all positive initial conditions. Right-hand panel: The ODE with the strong Allee effect only yields growth to the carrying capacity for initial conditions larger than the threshold value $\alpha > 0$. Initial conditions smaller than $\alpha > 0$ result in the extinction of w.

equations (ODEs)

$$\frac{dw}{dt} = f_{\text{logistic}}(w) = w(1-w) \quad \text{and} \quad \frac{dw}{dt} = f_{\text{Allee}}(w) = w(1-w)(w-\alpha). \tag{A.1}$$

Both ODEs are separable and can be solved analytically; sketches of the solutions are given in Fig. A1. The ODEs with logistic growth and the weak Allee effect yield growth (or decay) to the dimensionless carrying capacity ($w=1$) for any positive initial condition. In contrast, the ODE with the strong Allee effect yields growth (or decay) to the dimensionless carrying capacity only if an initial condition is greater than the threshold value $\alpha > 0$; initial conditions less than $\alpha > 0$ result in the extinction of the species.

The differences between logistic growth and the strong and weak Allee effects are further explained by looking at the *per capita growth rate* (pcgr) of w, in the absence of spatial (or other) effects. The pcgr of w is defined as

$$\text{pcgr}(w) := \frac{1}{w}\frac{dw}{dt} = \frac{d(\log w)}{dt},$$

where $\log w$ represents the natural logarithm of w. We determine the pcgr of w for the two cases, logistic and Allee, using dw/dt defined in (A.1):

$$\text{pcgr}_{\text{logistic}}(w) = 1-w, \quad \text{pcgr}_{\text{Allee}}(w) = (1-w)(w-\alpha).$$

Fig. A2 provides an illustration of these curves for $w \geq 0$.

For $0 < \alpha < 1$, the pcgr curve for the strong Allee effect is negative in a neighbourhood of $w=0$, before becoming positive at $w = \alpha$. This negativity, which corresponds to negative population growth, characterises the strong Allee effect. For $-1 < \alpha < 0$, the pcgr curve for the weak Allee effect decreases almost everywhere except for a small increasing part for $w \in [0, (1+\alpha)/2)$. This increase characterises the weak Allee effect.

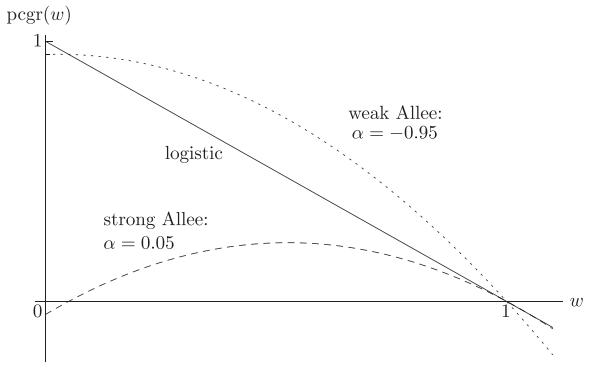

Fig. A2. The pcgr curves for logistic growth (solid), the strong Allee effect (dashed) and the weak Allee effect (dotted). The negativity of the dashed curve for $w < \alpha$ characterises the strong Allee effect. The turning point in the dotted curve at a *small* value of w relative to the carrying capacity (in this case, at $w = 1/40$), combined with the positive intercept (at $w=0$), characterises the weak Allee effect.

Appendix B. Results for the weak Allee model

The mathematical techniques outlined in Section 3 can be directly applied to the weak Allee model ((1)–(2) with $\alpha \gtrapprox -1$). With $\alpha < 0$, the equilibrium $(u, w) = (0, \alpha)$ lies on the negative w-axis and the equilibria $(u_\infty, 0)$ are centre stable, in contrast to the case presented in Section 3 with $\alpha > 0$. This means that the phase planes of the reduced problem in the weak and strong cases differ considerably, especially near the u-axis. In the weak case, trajectories can approach $(u_\infty, 0)$ via either the fast or slow dynamics, instead of only the fast. For $|\alpha|$ sufficiently large (see Remark 5), one canard point exists on F: a folded saddle. The left-hand panel of Fig. B1 illustrates these features and depicts an example phase plane for the weak Allee model.

The configuration of canard points and end states $(u_\infty, 0)$ for the weak Allee model is equivalent to that of the logistic model. Consequently, the analysis of the former is very similar to the latter, which is described in detail in Harley et al. (2014a). By glueing together trajectories of the reduced and layer problems, as in Section 3.4, we construct a family of Type I–IV travelling wave solutions, parametrised by c, for a given u_∞ and $\varepsilon = 0$. The Type III waves correspond to solutions that approach $(u_\infty, 0)$ via the fast dynamics, similar to the Type III waves in the strong Allee model. The Type I, II and IV waves correspond to solutions that approach $(u_\infty, 0)$ via the slow dynamics.

The persistence of these solutions follows from geometric singular perturbation theory and canard theory, using very similar arguments to those presented in Harley et al. (2014a). One difference arises from a *transversality condition*, which is automatically satisfied in the logistic model but is violated in the weak Allee model if $u_- = u_+ = c/\sqrt{1+\alpha}$, where $u_\pm$ is the u-coordinate of the shock; see Section 3.2. The full implications of this loss of transversality remain to be determined. One immediate implication is the breakdown of the proof of persistence for $0 < \varepsilon \ll 1$ for any travelling wave solutions that violate the transversality condition. Another implication appears to be the existence of non-unique solutions, that is, two possible travelling wave solutions for a given α, c, u_∞ and $\varepsilon = 0$: one with a shock and one without. Numerical simulations of the weak Allee model with $0 < \varepsilon \ll 1$ suggest that the Type I–III waves are stable; see Fig. B2.

The right-hand panel of Fig. B1 provides a plot of the speed of the Type III waves c_{III} as a function of the background ECM density u_∞, for fixed $\alpha = -0.95$. This monotonically increasing relationship resembles the corresponding relationship for the logistic model, rather than the experimentally justified biphasic relationship.

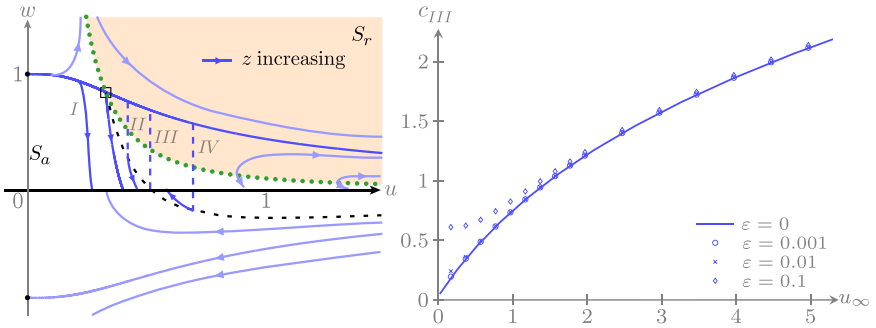

Fig. B1. Left-hand panel: Phase plane of (18), parametrised by z, with $\alpha = -0.95$, $c = 0.43$. The green line is the fold curve (F), which is dotted to illustrate its singularity. Black dots represent equilibria. The black open square is a folded saddle. F divides S into a repelling side (S_r, shaded) and an attracting side (S_a, unshaded). There exists a family of heteroclinic connections corresponding to Type I–IV travelling wave solutions. Right-hand panel: The relationship between the background ECM density (u_∞) and the speed of a Type III wave (c_{III}), with $\alpha = -0.95$. The solid curve is obtained from ODE simulations of (19); the markers are obtained from PDE simulations of the weak Allee model. (For interpretation of the references to color in this figure caption, the reader is referred to the web version of this paper.)

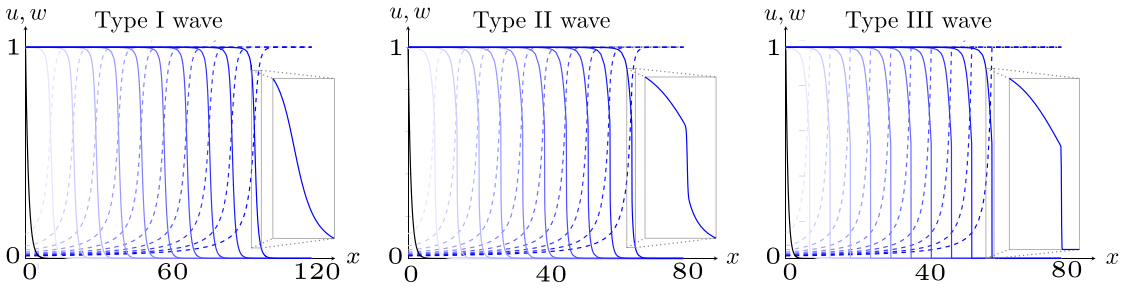

Fig. B2. Type I–III waves with speeds $c \approx 1.2, 0.80$ and 0.73, respectively, obtained by numerically simulating (1) with $\varepsilon = 0.001$, $\alpha = -0.95$ and $\beta = 0.5$. The only imposed difference between the three simulations is the initial condition, in particular, the steepness of the w-component; steeper w-components lead to slower waves. The dashed lines correspond to u-profiles and the solid lines to w-profiles, with solutions plotted at $t = 0$ (black), 8 (lightest), 16,…, 80 (darkest).

Remark 5. The above discussion of the weak Allee effect requires $|\alpha|$ to be sufficiently large. This ensures that there exists exactly one canard point on F. For $-7+4\sqrt{3} \approx -0.072 < \alpha < 0$, there may exist three canard points on F, depending on the value of c. As c increases, the number of canard points on F changes from one to three and back to one via two saddle-node bifurcations. Although this regime may be mathematically interesting, it is not biologically relevant since the weak Allee effect requires $\alpha \gtrapprox -1$; see Appendix A. Consequently, we do not consider it here.

Appendix C. Dimensionless variables and parameters

$$[u] = [\hat{u}]\frac{[k_4]}{[k_1][k_2]} = \frac{\mathrm{kg}}{\mathrm{m}^3} \times \frac{\mathrm{m}^6}{\mathrm{kg} \times \mathrm{cells} \times \mathrm{s}} \times \frac{\mathrm{cells} \times \mathrm{s}}{\mathrm{m}^3} = 1$$

$$[w] = [\hat{w}]\frac{1}{[k_2]} = \frac{\mathrm{cells}}{\mathrm{m}^3} \times \frac{\mathrm{m}^3}{\mathrm{cells}} = 1$$

$$[x] = [\hat{x}]\sqrt{\frac{[k_2][k_4]}{[k_3]}} = \mathrm{m} \times \sqrt{\frac{\mathrm{cells}}{\mathrm{m}^3} \times \frac{\mathrm{m}^6}{\mathrm{kg} \times \mathrm{cells} \times \mathrm{s}} \times \frac{\mathrm{kg} \times \mathrm{s}}{\mathrm{m}^5}} = 1$$

$$[t] = [\hat{t}][k_1][k_2]^2 = \mathrm{s} \times \frac{\mathrm{m}^3}{\mathrm{cells} \times \mathrm{s}} \times \frac{\mathrm{cells}}{\mathrm{m}^3} = 1$$

$$[\alpha] = \frac{[k_6]}{[k_2]} = \frac{\mathrm{cells}}{\mathrm{m}^3} \times \frac{\mathrm{m}^3}{\mathrm{cells}} = 1$$

$$[\beta] = \frac{[D_1]}{[D_2]} = \frac{\mathrm{m}^2}{\mathrm{s}} \times \frac{\mathrm{s}}{\mathrm{m}^2} = 1$$

$$[\varepsilon] = \frac{[k_4]}{[k_1][k_2][k_3]}[D_2] = \frac{\mathrm{m}^6}{\mathrm{kg} \times \mathrm{cells} \times \mathrm{s}} \times \frac{\mathrm{cells} \times \mathrm{s}}{\mathrm{m}^3} \times \frac{\mathrm{kg} \times \mathrm{s}}{\mathrm{m}^5} \times \frac{\mathrm{m}^2}{\mathrm{s}} = 1$$

Appendix D. Transversality

The curves J and T_o intersect at $(u, w) = (u_\infty, c^2/u_\infty^2)$. Since T_o follows the vector field, this intersection is transverse (not tangent) if

$$\left.\frac{\mathrm{d}J}{\mathrm{d}u}\right|_{u=u_\infty} - \left.\frac{\mathrm{d}w}{\mathrm{d}u}\right|_{(u,w)=(u_\infty, c^2/u_\infty^2)} \neq 0,$$

where $\mathrm{d}w/\mathrm{d}u$ is the ratio of the ODEs in (19). A straightforward computation shows that the above express is given by

$$\frac{2c^2}{u_\infty^3} + \frac{c^2(1-c^2/u_\infty^2)(c^2/u_\infty^2-\alpha) - 2u_\infty^3 c^4/u_\infty^4}{u_\infty^2(2u_\infty^2 c^2/u_\infty^2 - c^2)} = \frac{(u_\infty^2 - c^2)(c^2 - \alpha u_\infty^2)}{u_\infty^6} \neq 0.$$

So, transversality is lost if $c = u_\infty$ or $c = \sqrt{\alpha}\, u_\infty$. The former case implies that the take-off point of the jump is $(u, w) = (c, 1)$, which is only possible if $c = 0$. Thus, given $u_\infty, c > 0$, transversality is violated only if $c = \sqrt{\alpha}\, u_\infty$. This speed corresponds to a take-off point of the jump at $(u, w) = (u_\infty, \alpha)$.

References

Allee, W., 1938. The Social Life of Animals. Norton, New York.
Amar, M.B., Chatelain, C., Ciarletta, P., 2011. Contour instabilities in early tumor growth models. Phys. Rev. Lett. 106, 148101.
Amor, D., Solé, R., 2014. Catastrophic shifts and lethal thresholds in a propagating front model of unstable tumor progression. Phys. Rev. E 90, 022710.
Angulo, E., Roemer, E., Berec, L., Gascoigne, J., Courchamp, F., 2007. Double Allee effects and extinction in the island fox. Conserv. Biol. 21, 1082–1091.
Axelrod, R., Axelrod, D., Pienta, K., 2006. Evolution of cooperation among tumor cells. Proc. Natl. Acad. Sci. U. S. A. 103, 13474–13479.
Balasuriya, S., 2010. Invasions with density-dependent ecological parameters. J. Theor. Biol. 266, 657–666.
Balasuriya, S., Gottwald, G., 2010. Wavespeed in reaction-diffusion systems, with applications to chemotaxis and population pressure. J. Math. Biol. 61, 377–399.
Bellomo, N., Bellouquid, A., Nieto, J., Soler, J., 2010. Multiscale biological tissue models and flux-limited chemotaxis for multicellular growing systems. Math. Models Methods Appl. Sci. 20, 1179–1207.
Benoit, E., Callot, J.L., Diener, F., Diener, M., 1981. Chasse au canards. Collect. Math. 31, 37–119.
Berger, J., 1990. Persistence of different-sized populations: an empirical assessment of rapid extinctions in bighorn sheep. Conserv. Biol. 4, 91–98.
Bertuzzi, A., Fasano, A., Gandolfi, A., Sinisgalli, C., 2010. Necrotic core of EMT6/Ro tumour spheroids: is it caused by an ATP deficit?. J. Theor. Biol. 262, 142–150.
Böttger, K., Hatzikirou, H., Voss-Böhme, A., Cavalcanti-Adam, E.A., Herrero, M.A., Deutsch, A., 2015. An emerging Allee effect is critical for tumor initiation and persistence. PLoS Comput. Biol. 11 (9), e1004366.
Burrell, R., McGranahan, N., Bartek, J., Swanton, C., 2013. The causes and consequences of genetic heterogeneity in cancer evolution. Nature 501, 338–345.
Chaplain, M., Lachowics, M., Szymanska, Z., Wrzosek, D., 2011. Mathematical modelling of cancer invasion: the importance of cell-cell adhesion and cell-matrix adhesion. Math. Models Methods Appl. Sci. 21, 719–743.
Connolly, J., Schnitt, S., Stuart, J., Wang, H., Dvorak, A., Dvorak, H., 2000. Principles of cancer pathology. In: Bast, R., Kufe, D., Pollock, R., Weichselbaum, R., Holland, J., Frei, I. (Eds.), Cancer Medicine. BC Dekker, Hamilton, ON, pp. 533–555 (Chapter 29).
Courchamp, F., Berec, L., Gascoigne, J., 2008. Allee Effects in Ecology and Conservation. Oxford University Press, Oxford.
Courchamp, F., Clutton-Block, T., Grenfell, B., 1999. Inverse density dependence and the Allee effect. Trends Ecol. Evol. 14, 405–410.
Courchamp, F., MacDonald, D., 2001. Crucial importance of pack size in the African wild dog Lycaon pictus. Anim. Conserv. 4, 169–174.
Cushing, J., 2014. Backward bifurcations and strong Allee effects in matrix models for the dynamics of structured populations. J. Biol. Dyn. 8, 57–73.
Davis, H., Taylor, C., Civille, J., Strong, D., 2004. An Allee effect at the front of a plant invasion: spartina in a Pacific estuary. J. Ecol. 91, 321–327.
Engwer, C., Hillen, T., Knappitsch, M., Surulescu, C., 2015. Glioma follow white matter tracts: a multiscale DTI-based model. J. Math. Biol. 71, 551–582.
Fenichel, N., 1979. Geometric singular perturbation theory for ordinary, differential equations. J. Differ. Equ. 31, 53–98.
Gao, C., Xie, Q., Su, Y., Koeman, J., Khoo, S., Gustafson, M., Knudsen, B., Hay, R., Shinomiya, N., Van de Woude, G., 2005. Proliferation and invasion: plasticity in tumour cells. Proc. Natl. Acad. Sci. U. S. A. 120, 10528–10533.
Gatenby, R., Gawlinski, E., 1996. A reaction-diffusion model of cancer invasion. Cancer Res. 51, 5745–5753.
Gerisch, A., Chaplain, M., 2008. Mathematical modelling of cancer cell invasion of tissue: local and non-local models and the effect of adhesion. J. Theor. Biol. 250, 684–704.
Greaves, M., Maley, C., 2012. Clonal evolution in cancer. Nature 481, 306–313.
Gregory, S., Bradshaw, C., Brook, B., Courchamp, F., 2010. Limited evidence for the demographic Allee effect from numerous species across taxa. Ecology 91, 2151–2161.
Groom, M., 1998. Allee effects limit population viability of an annual plant. Am. Nat. 151, 487–496.
Harley, K., van Heijster, P., Marangell, R., Pettet, G.J., Wechselberger, M., 2014a. Existence of travelling wave solutions for a model of tumour invasion. SIAM J. Appl. Dyn. Syst. 13, 366–396.

Harley, K., van Heijster, P., Marangell, R., Pettet, G.J., Wechselberger, M., 2014b. Novel solutions for a model of wound healing angiogenesis. Nonlinearity 27, 2975–3003.
Harley, K., van Heijster, P., Marangell, R., Pettet, G.J., Wechselberger, M., 2015. Numerical computation of an Evans function for travelling waves. Math. Biosci. 266, 36–51.
Hart, E., Aviles, L., 2014. Reconstructing local population dynamics in noisy metapopulations–the role of random catastrophes and Allee effects. PLoS One 9, e110049.
Hatzikirou, H., Basanta, D., Simon, M., Schaller, K., Deutch, A., 2012. Go and grow: the key to the emergence of invasion in tumour progression?. Math. Med. Biol. 29, 49–65.
Hek, G., 2010. Geometric singular perturbation theory in biological practice. J. Math. Biol. 60, 347–386.
Johnson, D., Liebhold, A., Tobin, P., Bjornstad, O., 2006. Allee effects and pulsed invasion by the gypsy moth. Nature 444, 361–363.
Jones, C.K.R.T., 1995. Dynamical Systems. Geometric Singular Perturbation Theory, vol. 1609. Springer, Berlin/Heidelberg, pp. 44–118.
Kaper, T.J., 1999. An introduction to geometric methods and dynamical systems theory for singular perturbation problems. In: Proceedings of Symposia in Applied Mathematics, 56. American Mathematical Society, Baltimore, Maryland, pp. 85–132.
Keitt, T., Lewis, M., Holt, R., 2001. Allee effects, invasion pinning, and species' borders. Am. Nat. 157, 203–216.
Korolev, K., Xavier, J., Gore, J., 2014. Turning ecology and evolution against cancer. Nat. Rev. Cancer 14, 371–379.
Kramer, A., Dennis, B., Liebhold, A., Drake, J., 2009. The evidence for Allee effects. Popul. Ecol. 51, 341–354.
Kribs-Zaleta, C., Mitchell, C., 2014. Modeling colony collapse disorder in honeybees as a contagion. Math. Biosci. Eng. 11, 1275–1294.
Krupa, M., Szmolyan, P., 2001. Extending geometric singular perturbation theory to nonhyperbolic points–fold and canard points in two dimensions. SIAM J. Math. Anal. 33, 286–314.
Kuznetsov, Y.A., 2004. Elements of Applied Bifurcation Theory, 3rd ed. Springer, New York.
Lamont, B., Klinkhamer, P., Witkowski, E., 1993. Population fragmentation may reduce fertility to zero in Banksia-Goodii: a demonstration of the Allee effect. Oecologia 94, 446–450.
Lewis, M., Kareiva, P., 1993. Allee dynamics and the spread of invading organisms. Theor. Popul. Biol. 43, 141–158.
Machens, A., Holzhausen, H.-J., Henning, D., 2005. The prognostic value of primary tumor size in papillary and follicular thyroid carcinoma. Cancer 103, 2269–2273.
Marchant, B.P., Norbury, J., Byrne, H.M., 2006. Biphasic behaviour in malignant invasion. Math. Med. Biol. 23, 173–196.
Marchant, B.P., Norbury, J., Perumpanani, A.J., 2000. Traveling shock waves arising in a model of malignant invasion. SIAM J. Appl. Math. 60, 463–476.
Martínez-González, A., Calvo, G., Pérez Romasanta, L., Pérez-Garcia, V., 2012. Hypoxic cell waves around necrotic cores in glioblastoma: biomathematical model and its therapeutic implications. Bull. Math. Biol. 74, 2875–2896.
McGillen, J., Gaffney, E., Martin, N., Maini, P., 2014. A general reaction-diffusion model of acidity and cancer invasion. J. Math. Biol. 68, 1199–1224.
Merlo, L., Pepper, J., Reid, B., Maley, C., 2006. Cancer as an evolutionary and ecological process. Nat. Rev. Cancer 6, 924–935.
Michor, F., Iwasa, Y., Nowak, M., 2004. Dynamics of cancer progression. Nat. Rev. Cancer 4, 197–205.
Painter, K., Hillen, T., 2013. Mathematical modelling of glioma growth: the use of diffusion tensor imaging (DTI) data to predict the anisotropic pathways of cancer invasion. J. Theor. Biol. 323, 25–39.
Perumpanani, A.J., Byrne, H.M., 1999. Extracellular matrix concentration exerts selection pressure on invasive cells. Eur. J. Cancer 35, 1274–1280.
Perumpanani, A.J., Sherratt, J.A., Norbury, J., Byrne, H.M., 1999. A two parameter family of travelling waves with a singular barrier arising from the modelling of extracellular matrix mediated cellular invasion. Physica D 126, 145–159.
Pienta, K., McGregor, N., Axelrod, R., Axelrod, D., 2008. Ecological therapy for cancer: defining tumors using an ecosystem paradigm suggests new opportunities for novel cancer treatments. Transl. Oncol. 1, 158–164.
Potapov, A., Rajakaruna, H., 2013. Allee threshold and stochasticity in biological invasions: colonization time at low propagule pressure. J. Theor. Biol. 337, 1–14.
Ruppender, N., Morrisey, C., Lange, P., Vesella, R., 2013. Dormancy in solid tumors: implications for prostate cancer. Cancer Metast. Rev. 32, 501–509.
Sanderson, C., Jobbins, S., Alexander, K., 2014. With Allee effects, life for the social carnivore is complicated. Popul. Ecol. 56, 417–425.
Sherratt, J., Gourley, S., Armstrong, N., Painter, K., 2009. Boundedness of solutions of a non-local reaction-diffusion model for adhesion in cell aggregation and cancer invasion. Eur. J. Appl. Math. 20, 123–144.
Smith, R., Tan, C., Srimani, J., Pai, A., Riccione, K., Song, H., You, L., 2014. Programmed Allee effect in bacteria causes a tradeoff between population spread and survival. Proc. Natl. Acad. Sci. U. S. A. 111, 1969–1974.
Stephens, P., Sutherland, W., 1999. Consequences of the Allee effect for behaviour ecology and conservation. Trends Ecol. Evol. 14, 401–405.
Szmolyan, P., Wechselberger, M., 2001. Canards in $\mathbb{R}^3$. J. Differ. Equ. 177, 419–453.
Szymanska, Z., Rodrigo, C., Lachowicz, M., Chaplain, M., 2009. Mathematical modelling of cancer invasion of tissue: the role and effect of nonlocal interactions. Math. Models Methods Appl. Sci. 19, 257–281.
Tang, X., Meng, L., Kapranas, A., Xu, F., Hardy, I.C.W., Li, B., 2014. Mutually beneficial host exploitation and ultra-biased sex ratios in quasisocial parasitoids. Nat. Commun. 5, 4942.
Taylor, C., Davis, H., Civille, J., Grevstad, F., Hasting, A., 2004. Consequences of an Allee effect in the invasion of a Pacific estuary by *spartina alterniflora*. Ecology 85, 3254–3266.
Tektonidis, M., Hatzikirou, H., Chauvière, A., Simon, M., Schaller, K., Deutch, A., 2011. Identification of intrinsic in vitro cellular mechanisms for glioma invasion. J. Theor. Biol. 287, 131–147.
Tinevez, J.-Y., Schulze, U., Salbreux, G., Roensch, J., Joannu, J.-F., Paluch, E., 2009. Role of cortical tension in bleb growth. Proc. Natl. Acad. Sci. U. S. A. 106, 18581–18586.
Wechselberger, M., 2005. Existence and bifurcation of canards in $\mathbb{R}^3$ in the case of a folded node. SIAM J. Appl. Dyn. Syst. 4, 101–139.
Wechselberger, M., 2012. À propos de canards. Trans. Am. Math. Soc. 304, 3289–3309.
Wechselberger, M., Pettet, G.J., 2010. Folds, canards and shocks in advection-reaction-diffusion models. Nonlinearity 23, 1949–1969.
Wells, A., Grahovac, J., Wheeler, S., Ma, B., Lauffenburger, D., 2013. Targeting tumor cell motility as a strategy against invasion and metastasis. Trends Pharmocol. Sci. 34, 283–289.
Wittman, M., Gabriel, W., Metzler, D., 2014a. Genetic diversity in introduced populations with an Allee effect. Genetics 198, 299–310.
Wittman, M., Gabriel, W., Metzler, D., 2014b. Population genetic consequences of the Allee effect and the role of offspring-number variation. Genetics 198, 311–320.
Yamamichi, M., Yoshida, T., Sasaki, A., 2014. Timing and propagule size of invasion determine its success by a time-varying threshold of demographic regime shift. Ecology 95, 2303–2315.